bioRxiv preprint doi: https://doi.org/10.1101/051631; this version posted December 6, 2016. The copyright holder for this preprint (which was not certified by peer review) is the author/funder, who has granted bioRxiv a license to display the preprint in perpetuity. It is made available under aCC-BY-NC-ND 4.0 International license.

Visualizing the Structure of RNA-seq Expression Data using Grade of Membership Models

Kushal K Dey [1], Chiaowen Joyce Hsiao [2], Matthew Stephens[1,2]

1 Department of Statistics, University of Chicago, Chicago, Illinois 60637, USA
2 Department of Human Genetics, University of Chicago, Chicago, Illinois 60637, USA

* mstephens@uchicago.edu

Abstract

Grade of membership models, also known as "admixture models", "topic models" or "Latent Dirichlet Allocation", are a generalization of cluster models that allow each sample to have membership in multiple clusters. These models are widely used in population genetics to model admixed individuals who have ancestry from multiple "populations", and in natural language processing to model documents having words from multiple "topics". Here we illustrate the potential for these models to cluster samples of RNA-seq gene expression data, measured on either bulk samples or single cells. We also provide methods to help interpret the clusters, by identifying genes that are distinctively expressed in each cluster. By applying these methods to several example RNA-seq applications we demonstrate their utility in identifying and summarizing structure and heterogeneity. Applied to data from the GTEx project on 53 human tissues, the approach highlights similarities among biologically-related tissues and identifies distinctively-expressed genes that recapitulate known biology. Applied to single-cell expression data from mouse preimplantation embryos, the approach highlights both discrete and continuous variation through early embryonic development stages, and highlights genes involved in a variety of relevant processes – from germ cell development, through compaction and morula formation, to the formation of inner cell mass and trophoblast at the blastocyst stage. The methods are implemented in the Bioconductor package `CountClust`.

Author Summary

Gene expression profile of a biological sample (either from single cells or pooled cells) results from a complex interplay of multiple related biological processes. Consequently, for example, distal tissue samples may share a similar gene expression profile through some common underlying biological processes. Our goal here is to illustrate that grade of membership (GoM) models – an approach widely used in population genetics to cluster admixed individuals who have ancestry from multiple populations – provide an attractive approach for clustering biological samples of RNA sequencing data. The GoM model allows each biological sample to have partial memberships in multiple biologically-distinct clusters, in contrast to traditional clustering methods that partition samples into distinct subgroups. We also provide methods for identifying genes that are distinctively expressed in each cluster to help biologically interpret the results. Applied to a dataset of 53 human tissues, the GoM approach highlights similarities among biologically-related tissues and identifies distinctively-expressed genes that recapitulate

bioRxiv preprint doi: https://doi.org/10.1101/051631; this version posted December 6, 2016. The copyright holder for this preprint (which was not certified by peer review) is the author/funder, who has granted bioRxiv a license to display the preprint in perpetuity. It is made available under aCC-BY-NC-ND 4.0 International license.

known biology. Applied to gene expression data of single cells from mouse preimplantation embryos, the approach highlights both discrete and continuous variation through early embryonic development stages, and genes involved in a variety of relevant processes. Our study highlights the potential of GoM models for elucidating biological structure in RNA-seq gene expression data.

Introduction

Ever since large-scale gene expression measurements have been possible, clustering – of both genes and samples – has played a major role in their analysis [5–7]. For example, clustering of genes can identify genes that are working together or are co-regulated, and clustering of samples is useful for quality control as well as identifying biologically-distinct subgroups. A wide range of clustering methods have therefore been employed in this context, including distance-based hierarchical clustering, k-means clustering, and self-organizing maps (SOMs); see for example [8, 9] for reviews.

Here we focus on cluster analysis of samples, rather than clustering of genes (although our methods do highlight sets of genes that distinguish each cluster). Traditional clustering methods for this problem attempt to partition samples into distinct groups that show "similar" expression patterns. While partitioning samples in this way has intuitive appeal, it seems likely that the structure of a typical gene expression data set will be too complex to be fully captured by such a partitioning. Motivated by this, here we analyse expression data using grade of membership (GoM) models [10], which generalize clustering models to allow each sample to have partial membership in multiple clusters. That is, they allow that each sample has a proportion, or "grade" of membership in each cluster. Such models are widely used in population genetics to model admixture, where individuals can have ancestry from multiple populations [16], and in document clustering [41, 42] where each document can have membership in multiple topics. In these fields GoM models are often known as "admixture models", and "topic models" or "Latent Dirichlet Allocation" [41]. GoM models have also recently been applied to detect mutation signatures in cancer samples [38].

Although we are not the first to apply GoM-like models to gene expression data, previous applications have been primarily motivated by a specific goal, "cell type deconvolution", which involves using cell-type-specific expression profiles of marker genes to estimate the proportions of different cell types in a mixture [47, 49, 50]. Specifically, the GoM model we use here is analogous to – although different in detail from – blind deconvolution approaches [45, 46, 48] which estimate cell type proportions and cell type signatures jointly (see also [43, 44] for semi-supervised approaches). Our goal here is to demonstrate that GoM models can be useful much more broadly for understanding structure in RNA-seq data – not only to deconvolve mixtures of cell types. For example, in our analysis of human tissue samples from the GTEX project below, the GoM model usefully captures biological heterogeneity among samples even though the inferred grades of membership are unlikely to correspond precisely to proportions of specific cell types. And in our analyses of single-cell expression data the GoM model highlights interesting structure, even though interpreting the grades of membership as "proportions of cell types" is clearly inappropriate because each sample is a single cell! Here we are exploiting the GoM as a flexible extension of traditional cluster models, which can capture "continuous" variation among cells as well as the more "discrete" variation captured by cluster models. Indeed, the extent to which variation among cells can be described in terms of discrete clusters versus more continuous populations is a fundamental question that, when combined with appropriate single-cell RNA-seq data, the GoM models used here may ultimately help address.

bioRxiv preprint doi: https://doi.org/10.1101/051631; this version posted December 6, 2016. The copyright holder for this preprint (which was not certified by peer review) is the author/funder, who has granted bioRxiv a license to display the preprint in perpetuity. It is made available under aCC-BY-NC-ND 4.0 International license.

Methods Overview

We assume that the RNA-seq data on N samples has been summarized by a table of counts $C_{N\times G} = (c_{ng})$, where c_{ng} is the number of reads from sample n mapped to gene g (or other unit, such as transcript or exon) [14]. The GoM model is a generalization of a cluster model, which allows that each sample has some proportion ("grade") of membership, in each cluster. For RNA-seq data this corresponds to assuming that each sample n has some proportion of its reads, q_{nk} coming from cluster k. In addition, each cluster k is characterized by a probability vector, $\theta_{k\cdot}$, whose gth element represents the relative expression of gene g in cluster k. The GoM model is then

$$(c_{n1}, c_{n2}, \cdots, c_{nG}) \sim \text{Multinomial}\left(c_{n+}, p_{n1}, p_{n2}, \cdots, p_{nG}\right), \tag{1}$$

where

$$p_{ng} := \sum_{k=1}^{K} q_{nk}\theta_{kg}. \tag{2}$$

The number of clusters K is set by the analyst, and it can be helpful to explore multiple values of K (see Discussion).

To fit this model to RNA-seq data, we exploit the fact that this GoM model is commonly used for document clustering [41]. This is because, just as RNA-seq samples can be summarized by counts of reads mapping to each possible gene in the genome, document data can be summarized by counts of each possible word in a dictionary. Recognizing this allows existing methods and software for document clustering to be applied directly to RNA-seq data. Here we use the R package `maptpx` [15] to fit the GoM model.

Fitting the GoM model results in estimated membership proportions q for each sample, and estimated expression values θ for each cluster. We visualize the membership proportions for each sample using a "Structure plot" [17], which is named for its widespread use in visualizing the results of the *Structure* software [16] in population genetics. The Structure plot represents the estimated membership proportions of each sample as a stacked barchart, with bars of different colors representing different clusters. Consequently, samples that have similar membership proportions have similar amounts of each color. See Fig 1 for example.

To help biologically interpret the clusters inferred by the GoM model we also implemented methods to identify, for each cluster, which genes are most distinctively differentially expressed in that cluster; that is, which genes show the biggest difference in expression compared with the other most similar cluster (see Methods). Functions for fitting the GoM model, plotting the structure plots, and identifying the distinctive ("driving") genes in each cluster, are included in our R package `CountClust` [53] available through Bioconductor [36].

Results

Bulk RNA-seq data of human tissue samples

We begin by illustrating the GoM model on bulk RNA expression measurements from the GTEx project (V6 dbGaP accession phs000424.v6.p1, release date: Oct 19, 2015, `http://www.gtexportal.org/home/`). These data consist of per-gene read counts from RNA-seq performed on $8,555$ samples collected from 450 human donors across 53 tissues, lymphoblastoid cell lines, and transformed fibroblast cell-lines. We analyzed $16,069$ genes that satisfied filters (e.g. exceeding certain minimum expression levels) that were used during eQTL analyses by the GTEx project (gene list available in

bioRxiv preprint doi: https://doi.org/10.1101/051631; this version posted December 6, 2016. The copyright holder for this preprint (which was not certified by peer review) is the author/funder, who has granted bioRxiv a license to display the preprint in perpetuity. It is made available under aCC-BY-NC-ND 4.0 International license.

http://stephenslab.github.io/count-clustering/project/utilities/gene_names_all_gtex.txt).

We fit the GoM model to these data, with number of clusters $K = 5, 10, 15, 20$. For each K we ran the fitting algorithm three times and kept the result with the highest log-likelihood. As might be expected, increasing K highlights finer structure in the data, and for brevity we focus discussion on results for $K = 20$ (Fig 1(a)), with results for other K shown in S1 Fig. For comparison we also ran several other commonly-used methods for clustering and visualizing gene expression data: Principal Components Analysis (PCA), Multidimensional Scaling (MDS), t-Distributed Stochastic Neighbor Embedding (t-SNE) [25, 26], and hierarchical clustering (Fig 2).

These data present a challenge to visualization and clustering tools, because of both the relatively large number of samples and the complex structure created by the inclusion of many different tissues. Indeed, neither PCA nor MDS provide satisfactory summaries of the structure in these data (Fig 2(a,b)): samples from quite different tissues are often super-imposed on one another in plots of PC1 vs PC2, and this issue is only partly alleviated by examining more PCs (Supplementary Figure S2 Fig). The hierarchical clustering provides perhaps better separation of tissues (Fig 2(d)), but producing a clear (static) visualization of the tree is difficult with this many samples. By comparison t-SNE (Fig 2(b)) and the GoM model (Fig 1(a)) both show a much clearer visual separation of samples by tissue, although they achieve this in very different ways. The t-SNE representation produces a two-dimensional plot with 20-25 visually-distinct clusters. In contrast, the GoM highlights similarity among samples by assigning them similar membership proportions, resulting in groups of similarly-colored bars in the structure plot. Some tissues are represented by essentially a single cluster/color (e.g. Pancreas, Liver), whereas other tissues are represented as a mixture of multiple clusters (e.g. Thyroid, Spleen). Furthermore, the GoM results highlight biological similarity among some tissues by assigning similar membership proportions to samples from those tissues. For example, samples from several different parts of the brain often have similar memberships, as do the arteries (aorta, tibial and coronary) and skin samples (sun-exposed and un-exposed).

Although it is not surprising that samples cluster by tissue, other results could have occurred. For example, samples could have clustered according to technical variables, such as sequencing batch [34] or sample collection center. While our results do not exclude the possibility that technical variables could have influenced these data, the t-SNE and GoM results clearly demonstrate that tissue of origin is the primary source of heterogeneity, and provide a useful initial assurance of data quality.

While in these data both the GoM model and t-SNE highlight the primary structure due to tissue of origin, the GoM results have at least two advantages over t-SNE. First, the GoM model provides an explicit, quantitative, estimate of the mean expression of each gene in each cluster, making it straightforward to assess which genes and processes drive differences among clusters; see Table 1 (and also S1 Table). Reassuringly, many results align with known biology. For example, the purple cluster (cluster 18), which distinguishes Pancreas from other tissues, is enriched for genes responsible for digestion and proteolysis, (e.g. *PRSS1*, *CPA1*, *PNLIP*). Similarly the yellow cluster (cluster 12), which primarily distinguishes Cell EBV Lymphocytes from other tissues, is enriched with genes responsible for immune responses (e.g. *IGHM*, *IGHG1*) and the pink cluster (cluster 19) which mainly appears in Whole Blood, is enriched with genes related hemoglobin complex and oxygen transport (e.g. *HBB*, *HBA1*, *HBA2*). Further, Keratin-related genes characterize the skin cluster (cluster 6, light denim), Myosin-related genes characterize the muscle skeletal cluster (cluster 7, orange), etc. These biological annotations are particularly helpful for understanding instances where a cluster appears in multiple tissues. For example, the top genes in the salmon cluster

bioRxiv preprint doi: https://doi.org/10.1101/051631; this version posted December 6, 2016. The copyright holder for this preprint (which was not certified by peer review) is the author/funder, who has granted bioRxiv a license to display the preprint in perpetuity. It is made available under aCC-BY-NC-ND 4.0 International license.

(cluster 4), which is common to the Gastroesophageal Junction, Esophagus Muscularis and Colon Sigmoid, are related to smooth muscle. And the top genes in the red cluster, highlighted above as common to Breast Mammary tissue, Adipose Subcutaneous and Adipose Visceral, are all related to adipocytes and/or fatty acid synthesis.

A second advantage of the GoM model is that, because it allows partial membership in each cluster, it is better able to highlight partial similarities among distinct tissues. For example, in Figure 1(a) the sky blue cluster (cluster 13), appears in testis, pituitary, and thyroid, reflecting shared hormonal-related processes. At the same time, these tissues are distinguished from one another both by their degree of membership in this cluster (testis samples have consistently stronger membership; thyroid samples consistently weaker), and by membership in other clusters. For example, pituitary samples, but not testis or thyroid samples, have membership in the light purple cluster (cluster 2) which is driven by genes related to neurons and synapsis. In the *t*-SNE results these three tissues simply cluster separately into visually distinct groups, with no indication that their expression profiles have something in common (Fig 2(b)). Thus, although we find the *t*-SNE results visually attractive, this 2-dimensional projection contains less information than the Structure plot from the GoM (Fig 1(a)), which uses color to represent the samples in a 20-dimensional space.

In addition to these qualitative comparisons with other methods, we also used the GTEx data to quantitatively compare the accuracy of the GoM model with hierarchical clustering. Specifically, for each pair of tissues in the GTEx data we assessed whether or not each method correctly partitioned samples into the two tissue groups; see Methods. (Other methods do not provide an explicit clustering of the samples – only a visual representation – and so are not included in these comparisons.) The GoM model was more accurate in this test, succeeding in 88% of comparisons, compared with 79% for hierarchical clustering (Supplemental Figure S3 Fig (c) vs (a)).

Sub-analysis of Brain tissues

Although the analysis of all tissues is useful for assessing global structure, it may miss finer-scale structure within tissues or among similar tissues. For example, here the GoM model applied to all tissues effectively allocated only three clusters to all brain tissues (clusters 1,2 and 9 in Fig 1(a)), and we suspected that additional substructure might be uncovered by analyzing the brain samples separately and using more clusters. Fig 1(b) shows the Structure plot for $K = 6$ on only the Brain samples. The results highlight much finer-scale structure compared with the global analysis. Brain Cerebellum and Cerebellar hemisphere are essentially assigned to a separate cluster (lime green), which is enriched with genes related to cell periphery and communication (e.g. *PKD1*, *CBLN3*) as well as genes expressed largely in neuronal cells and playing a role in neuron differentiation (e.g. *CHGB*). The spinal cord samples also show consistently strong membership in a single cluster (yellow-orange), the top defining gene for the cluster being *MBP* which is involved in myelination of nerves in the nervous system [51]. Another driving gene, *GFAP*, participates in system development by acting as a marker to distinguish astrocytes during development [4].

The remaining samples all show membership in multiple clusters. Samples from the putamen, caudate and nucleus accumbens show similar profiles, and are distinguished by strong membership in a cluster (cluster 4, bright red) whose top driving gene is *PPP1R1B*, a target for dopamine. And cortex samples are distinguished from others by stronger membership in a cluster (cluster 2, turquoise in Fig 1(b)) whose distinctive genes include *ENC1*, which interacts with actin and contributes to the organisation of the cytoskeleton during the specification of neural fate [3].

In comparison, applying PCA, MDS, hierarchical clustering and *t*-SNE to these brain samples reveals less of this finer-scale structure (Supplementary Figures S4 Fig).

bioRxiv preprint doi: https://doi.org/10.1101/051631; this version posted December 6, 2016. The copyright holder for this preprint (which was not certified by peer review) is the author/funder, who has granted bioRxiv a license to display the preprint in perpetuity. It is made available under aCC-BY-NC-ND 4.0 International license.

Both PCA and MDS effectively cluster the samples into two groups – those related to the cerebellum vs everything else. Hierarchical clustering also separates out the cerebellum-related tissues from the others, but again the format seems ill-suited to static visualization of more than one thousand samples. For reasons that we do not understand t-SNE performs poorly for these data: many samples are allocated to essentially identical locations, and so overplotting obscures them.

Single-cell RNA-seq data

Recently RNA-sequencing has become viable for single cells [11], and this technology has the promise to revolutionize understanding of intra-cellular variation in expression, and regulation more generally [12]. Although it is traditional to describe and categorize cells in terms of distinct cell-types, the actual architecture of cell heterogeneity may be more complex, and in some cases perhaps better captured by the more "continuous" GoM model. In this section we illustrate the potential for the GoM model to be applied to single cell data.

To be applicable to single-cell RNA-seq data, methods must be able to deal with lower sequencing depth than in bulk RNA experiments: single-cell RNA-seq data typically involve substantially lower effective sequencing depth compared with bulk experiments, due to the relatively small number of molecules available to sequence in a single cell. Therefore, as a first step towards demonstrating its potential for single cell analysis, we checked robustness of the GoM model to sequencing depth. Specifically, we repeated the analyses above after thinning the GTEx data by a factor of 100 and $10,000$ to mimic the lower sequencing depth of a typical single cell experiment. For the thinned GTEx data the Structure plot for $K = 20$ preserves most of the major features of the original analysis on unthinned data (Supplemental Figure S5 Fig). For the accuracy comparisons with hierarchical clustering, both methods suffer reduced accuracy in thinned data, but the GoM model remains superior (Supplemental Figure S6 Fig). For example, when thinning by a factor of $10,000$, the success rate in separating pairs of tissues is 0.32 for the GoM model vs 0.10 for hierarchical clustering.

Having established its robustness to sequencing depth, we now illustrate the GoM model on two single cell RNA-seq datasets: data on mouse spleen from Jaitin *et al* [27] and data on mouse preimplantation embryos from Deng *et al* [28].

Mouse Spleen data from Jaitin et al, 2014

Jaitin *et al* sequenced over $4,000$ single cells from mouse spleen. Here we analyze $1,041$ of these cells that were categorized as $CD11c+$ in the *sorting markers* column of their data (`http://compgenomics.weizmann.ac.il/tanay/?page_id=519`), and which had total number of reads mapping to non-ERCC genes greater than 600. Our hope was that applying the GoM model to these data would identify, and perhaps refine, the cluster structure evident in [27] (their Fig 2A and 2B). However, the GoM model yielded rather different results (Fig 3), where most cells were assigned to have membership in several clusters. Further, the cluster membership vectors showed systematic differences among amplification batches (which in these data is also strongly correlated with sequencing batch). For example, cells in batch 1 are characterized by strong membership in the orange cluster (cluster 5) while those in batch 4 are characterized by strong membership in both the blue and yellow clusters (2 and 6). Some adjacent batches show similar patterns - for example batches 28 and 29 have a similar visual "palette", as do batches 32-45. And, more generally, these later batches are collectively more similar to one another than they are to the earlier batches (0-4).

The fact that batch effects are detectable in these data is not particularly surprising: there is a growing recognition of the importance of batch effects in high-throughput

bioRxiv preprint doi: https://doi.org/10.1101/051631; this version posted December 6, 2016. The copyright holder for this preprint (which was not certified by peer review) is the author/funder, who has granted bioRxiv a license to display the preprint in perpetuity. It is made available under aCC-BY-NC-ND 4.0 International license.

data generally [31, 32] and in single cell data specifically [33, 34]. And indeed, both clustering methods and the GoM model can be viewed as dimension reduction methods, and such methods can be helpful in controlling for batch effects [29, 30]. However, why these batch effects are not evident in Fig 2A and 2B of [27] is unclear.

Mouse preimplantation embryo data from Deng et al, 2014

Deng *et al* collected single-cell expression data of mouse preimplantation embryos from the zygote to blastocyst stage [28], with cells from four different embryos sequenced at each stage. The original analysis [28] focuses on trends of allele-specific expression in early embryonic development. Here we use the GoM model to assess the primary structure in these data without regard to allele-specific effects (i.e. combining counts of the two alleles). Visual inspection of the Principal Components Analysis in [28] suggested perhaps 6-7 clusters, and we focus here on results with $K = 6$.

The results from the GoM model (Fig 4) clearly highlight changes in expression profiles that occur through early embryonic development stages, and enrichment analysis of the driving genes in each cluster (Table 3, S4 Table) indicate that many of these expression changes reflect important biological processes during embryonic preimplantation development.

In more detail: Initially, at the zygote and early 2-cell stages, the embryos are represented by a single cluster (blue in Fig 4) that is enriched with genes responsible for germ cell development (e.g., *Bcl2l10* [62], *Spin1* [63]). Moving through subsequent stages the grades of membership evolve to a mixture of blue and magenta clusters (mid 2-cell), a mixture of magenta and yellow clusters (late 2-cell) and a mixture of yellow and green (4-cell stage). The green cluster then becomes more prominent in the 8-cell and 16-cell stages, before dropping substantially in the early and mid-blastocyst stages. That is, we see a progression in the importance of different clusters through these stages, from the blue cluster, moving through magenta and yellow to green. Examining the genes distinguishing each cluster reveals that this progression (blue-magenta-yellow-green) reflects the changing relative importance of several fundamental biological processes. The magenta cluster is driven by genes responsible for the beginning of transcription of zygotic genes (e.g., *Zscan4c-f* show up in the list of top 100 driving genes : see `https://stephenslab.github.io/count-clustering/project/src/deng_cluster_annotations.html`), which takes place in the late 2-cell stage of early mouse embryonic development [65]. The yellow cluster is enriched for genes responsible for heterochromation *Smarcc1* [66] and chromosome stability *Cenpe* [67] (see S4 Table) . And the green cluster is enriched for cytoskeletal genes (e.g., *Fbxo15*) and cytoplasm genes (e.g., *Tceb1*, *Hsp90ab1*), all of which are essential for compaction at the 8-cell stage and morula formation at the 16-cell stage.

Finally, during the blastocyst stages two new clusters (purple and orange in Fig 4) dominate. The orange cluster is enriched with genes involved in the formation of trophectoderm (TE) (e.g., *Tspan8*, *Krt8*, *Id2* [59]), while the purple cluster is enriched with genes responsible for the formation of inner cell mass (ICM) (e.g., *Pdgfra*, *Pyy* [61]).

For comparison, results for PCA, MDS, t-SNE and hierarchical clustering are shown in Supplemental Figure S7 Fig. All these methods show some clustering structure by pre-implantation stage; however only PCA and MDS seem to capture the developmental trajectory from zygote to blastocyst, exhibiting a "horse-shoe" pattern that is expected when similarities among samples approximately reflect an underlying latent ordering [39, 40]. And none of them provide any direct indication of the ICM vs TE structure in the blastocyst samples.

Although the GoM model results clearly highlight some of the key biological processes underlying embryonic preimplantation development, there are also some

bioRxiv preprint doi: https://doi.org/10.1101/051631; this version posted December 6, 2016. The copyright holder for this preprint (which was not certified by peer review) is the author/funder, who has granted bioRxiv a license to display the preprint in perpetuity. It is made available under aCC-BY-NC-ND 4.0 International license.

expected patterns that do not appear. Specifically, just prior to implantation the embryo consists of three different cell types, the trophectoderm (TE), the primitive endoderm (PE), and the epiblast (EPI) [60], with the PE and EPI being formed from the ICM. Thus one might expect the late blastocyst cells to show a clear division into three distinct groups, and for some of the earlier blastocyst cells to show partial membership in one of these groups as they begin to differentiate towards these cell types. Indeed, the GoM model seems well suited to capture this process in principle. However, this is not the result we obtained in practice. In particular, although the two clusters identified by the GoM model in the blastocyst stages appear to correspond roughly to the TE and ICM, even the late blastocyst cells tend to show a gradient of memberships in both these clusters, rather than a clear division into distinct groups. Our results contrast with those from the single-cell mouse preimplantation data of [59], measured by qPCR, where the late blastocyst cells showed a clear visual division into three groups using PCA (their Figure 1).

To better understand the differences between our results for RNA-seq data from [28] and the qPCR results from [59] we applied the GoM model with $K = 3$ to a small subset of the RNA-seq data: the blastocyst cell data at the 48 genes assayed by [59]. These genes were specifically chosen by them to help elucidate cell-fate decisions during early development of the mouse embryo. Still, the GoM model results (Supplemental Figure S8 Fig) do not support a clear division of these data into three distinct groups (and neither do PCA or t-SNE; Supplemental Figure S9 Fig). Rather, the GoM model highlights one cluster (Green in figure), whose membership proportions essentially reflect expression at the *Actb* gene, and two other clusters (Orange and Purple in figure) whose driving genes correspond to genes identified in [59] as being distinctive to TE and EPI cell types respectively. The *Actb* gene is a "housekeeping gene", used by [59] to normalize their qPCR data, and its prominence in the GoM results likely reflects its very high expression levels relative to other genes. However, excluding *Actb* from the analysis still does not lead to a clear separation into three groups (Supplemental Figure S8 Fig). Thus, although there are clear commonalities in the structure of these RNA-seq and qPCR data sets, the structure of the single-cell RNA-seq data from [28] is fundamentally more complex (or, perhaps, muddied), and consequently more difficult to interpret.

In addition to trends across development stages, the GoM results also highlight some embryo-level effects in the early stages (Fig 4). Specifically, cells from the same embryo sometimes show greater similarity than cells from different embryos. For example, while all cells from the 16-cell stage have high memberships in the green cluster, cells from two of the embryos at this stage have memberships in both the purple and yellow clusters, while the other two embryos have memberships only in the yellow cluster.

The GoM results also highlight a few single cells as outliers. For example, a cell from a 16-cell embryo is represented by the blue cluster - a cluster that represents cells at the zygote and early 2-cell stage. Also, a cell from an 8-stage embryo has strong membership in the purple cluster - a cluster that represents cells from the blastocyst stage. This illustrates the potential for the GoM model to help in quality control: it would seem prudent to consider excluding these outlier cells from subsequent analyses of these data.

Discussion

Our goal here is to highlight the potential for GoM models to elucidate structure in RNA-seq data from both single cell sequencing and bulk sequencing of pooled cells. We also provide tools to identify which genes are most distinctively expressed in each cluster, to aid interpretation of results. As our applications illustrate, the results can provide a richer summary of the structure in RNA-seq data than existing widely-used visualization methods such as PCA and hierarchical clustering. While it could be

bioRxiv preprint doi: https://doi.org/10.1101/051631; this version posted December 6, 2016. The copyright holder for this preprint (which was not certified by peer review) is the author/funder, who has granted bioRxiv a license to display the preprint in perpetuity. It is made available under aCC-BY-NC-ND 4.0 International license.

argued that the GoM model results sometimes raise more questions than they answer, this is exactly the point of an exploratory analysis tool: to highlight issues for investigation, identify anomalies, and generate hypotheses for future testing.

Our results from different methods also highlight another important point: different methods have different strengths and weaknesses, and can compliment one another as well as competing. For example, t-SNE seems to provide a much clearer indication of the cluster structure in the full GTEx data than does PCA, but does a poorer job of capturing the ordering of the developmental samples from mouse pre-implantation embryos. While we believe the GoM model often provides a richer summary of the sample structure, we would expect to use it in addition to t-SNE and PCA when performing exploratory analyses. (Indeed the methods can be used in combination: both PCA and t-SNE can be used to visualize the results of the GoM model, as an alternative or complement to the Structure plot.)

A key feature of the GoM model is that it allows that each sample has a proportion of membership in each cluster, rather than a discrete cluster structure. Consequently it can provide insights into how well a particular dataset really fits a "discrete cluster" model. For example, consider the results for the data from Jaitin *et al* [27] and Deng *et al* [28]: in both cases most samples are assigned to multiple clusters, although the results are closer to "discrete" for the latter than the former. The GoM model is also better able to represent the situation where there is not really a single clustering of the samples, but where samples may cluster differently at different genes. For example, in the GTEx data, the stomach samples share memberships in common with both the pancreas (purple) and the adrenal gland (light green). This pattern can be seen in the Structure plot (Fig 1) but not from other methods like PCA, t-SNE or hierarchical clustering (Fig 2).

Fitting GoM models can be computationally-intensive for large data sets. For the datasets we considered here the computation time ranged from 12 minutes for the data from [28] ($n = 259; K = 6$), through 33 minutes for the data from [27] ($n = 1,041; K = 7$) to $3,370$ minutes for the GTEx data ($n = 8,555; K = 20$). Computation time can be reduced by fitting the model to only the most highly expressed genes, and we often use this strategy to get quick initial results for a dataset. Because these methods are widely used for clustering very large document datasets there is considerable ongoing interest in computational speed-ups for very large datasets, with "on-line" (sequential) approaches capable of dealing with millions of documents [56] that could be useful in the future for very large RNA-seq datasets.

A thorny issue that arises when fitting clustering models is how to select the number of clusters, K. Like many software packages for fitting these models, the `maptpx` package implements a measure of model fit that provides one useful guide. However, it is worth remembering that in practice there is unlikely to be a "true" value of K, and results from different values of K may complement one another rather than merely competing with one another. For example, seeing how the fitted model evolves as K increases is one way to capture some notion of hierarchy in the clusters identified [17]. More generally it is often fruitful to analyse data in multiple ways using the same tool: for example our GTEx analyses illustrate how analysis of subsets of the data (in this case the brain samples) can complement analyses of the entire data. Finally, as a practical matter, we note that Structure plots can be difficult to read for large K (e.g. $K = 30$) because of the difficulties of choosing a palette with K distinguishable colors.

The version of the GoM model fitted here is relatively simple, and could certainly be embellished. For example, the model allows the expression of each gene in each cluster to be a free parameter, whereas we might expect expression of most genes to be "similar" across clusters. This is analogous to the idea in population genetics applications that allele frequencies in different populations may be similar to one

bioRxiv preprint doi: https://doi.org/10.1101/051631; this version posted December 6, 2016. The copyright holder for this preprint (which was not certified by peer review) is the author/funder, who has granted bioRxiv a license to display the preprint in perpetuity. It is made available under aCC-BY-NC-ND 4.0 International license.

another [20], or in document clustering applications that most words may not differ appreciably in frequency in different topics. In population genetics applications incorporating this idea into the model, by using a correlated prior distribution on these frequencies, can help improve identification of subtle structure [20] and we would expect the same to happen here for RNA-seq data.

Finally, GoM models can be viewed as one of a larger class of "matrix factorization" approaches to understanding structure in data, which also includes PCA, non-negative matrix factorization (NMF), and sparse factor analysis (SFA); see [21]. This observation raises the question of whether methods like SFA might be useful for the kinds of analyses we performed here. (NMF is so closely related to the GoM model that we do not discuss it further; indeed, the GoM model is a type of NMF, because both grades of membership and expression levels within each cluster are required to be non-negative.) Informally, SFA can be thought of as a generalization of the GoM model that allows samples to have *negative* memberships in some "clusters" (actually, "factors"). This additional flexibility should allow SFA to capture certain patterns more easily than the GoM model. For example, a small subset of genes that are over-expressed in some samples and under-expressed in other samples could be captured by a single sparse factor, with positive loadings in the over-expressed samples and negative loadings in the other samples. However, this additional flexibility also comes at a cost of additional complexity in visualizing the results. For example, Supplementary Figures S10 Fig, S11 Fig, S12 Fig show results of SFA (the version from [21]) for the GTEx data and the mouse preimplantation data: in our opinion, these do not have the simplicity and immediate visual appeal of the GoM model results. Also, applying SFA to RNA-seq data requires several decisions to be made that can greatly impact the results: what transformation of the data to use; what method to induce sparsity (there are many; e.g. [21–24]); whether to induce sparsity in loadings, factors, or both; etc. Nonetheless, we certainly view SFA as complementing the GoM model as a promising tool for investigating the structure of RNA-seq data, and as a promising area for further work.

Methods and Materials

Model Fitting

We use the `maptpx` R package [15] to fit the GoM model (1,2), which is also known as "Latent Dirichlet Allocation" (LDA). The `maptpx` package fits this model using an EM algorithm to perform Maximum a posteriori (MAP) estimation of the parameters q and θ. See [15] for details.

Visualizing Results

In addition to the Structure plot, we have also found it useful to visualize results using t-distributed Stochastic Neighbor Embedding (t-SNE), which is a method for visualizing high dimensional datasets by placing them in a two dimensional space, attempting to preserve the relative distance between nearby samples [25, 26]. Compared with the Structure plot our t-SNE plots contain less information, but can better emphasize clustering of samples that have similar membership proportions in many clusters. Specifically, t-SNE tends to place samples with similar membership proportions together in the two-dimensional plot, forming visual "clusters" that can be identified by eye (e.g. `http://stephenslab.github.io/count-clustering/project/src/tissues_tSNE_2.html`). This may be particularly helpful in settings where no external information is available to aid in making an informative Structure plot.

bioRxiv preprint doi: https://doi.org/10.1101/051631; this version posted December 6, 2016. The copyright holder for this preprint (which was not certified by peer review) is the author/funder, who has granted bioRxiv a license to display the preprint in perpetuity. It is made available under aCC-BY-NC-ND 4.0 International license.

Cluster annotation

To help biologically interpret the clusters, we developed a method to identify which genes are most distinctively differentially expressed in each cluster. (This is analogous to identifying "ancestry informative markers" in population genetics applications [18].) Specifically, for each cluster k we measure the distinctiveness of gene g with respect to any other cluster l using

$$\mathrm{KL}^g[k,l] := \theta_{kg}\ log\frac{\theta_{kg}}{\theta_{lg}} + \theta_{lg} - \theta_{kg}, \tag{3}$$

which is the Kullback–Leibler divergence of the Poisson distribution with parameter θ_{kg} to the Poisson distribution with parameter θ_{lg}. For each cluster k, we then define the distinctiveness of gene g as

$$D^g[k] = \min_{l \neq k} \mathrm{KL}^g[k,l]. \tag{4}$$

The higher $D^g[k]$, the larger the role of gene g in distinguishing cluster k from all other clusters. Thus, for each cluster k we identify the genes with highest $D^g[k]$ as the genes driving the cluster k. We annotate the biological functions of these individual genes using the `mygene` R Bioconductor package [35].

For each cluster k, we filter out a number of genes (top 100 for the Deng *et al* data [28] and GTEx V6 data [13]) with highest $D^g[k]$ value and perform a gene set over-representation analysis of these genes against all the other genes in the data representing the background. To do this, we used ConsensusPathDB database (`http://cpdb.molgen.mpg.de/`) [57] [58]. See Table 1-2 and Table 3 for the top significant gene ontologies driving each cluster in the GTEx V6 data and the Deng *et al* data respectively.

Comparison with hierarchical clustering

We compared the GoM model with a distance-based hierarchical clustering algorithm by applying both methods to samples from pairs of tissues from the GTEx project, and assessed their accuracy in separating samples according to tissue. For each pair of tissues we randomly selected 50 samples from the pool of all samples coming from these tissues. For the hierarchical clustering approach we cut the dendrogram at $K = 2$, and checked whether or not this cut partitions the samples into the two tissue groups. (We applied hierarchical clustering using Euclidean distance, with both complete and average linkage; results were similar and so we showed results only for complete linkage.)

For the GoM model we analysed the data with $K = 2$, and sorted the samples by their membership in cluster 1. We then partitioned the samples at the point of the steepest fall in this membership, and again we checked whether this cut partitions the samples into the two tissue groups. Supplemental Figure S3 Fig shows, for each pair of tissues, whether each method successfully partitioned the samples into the two tissue groups.

Thinning

We used "thinning" to simulate lower-coverage data from the original higher-coverage data.. Specifically, if c_{ng} is the counts of number of reads mapping to gene g for sample n for the original data, we simulated thinned counts t_{ng} using

$$t_{ng} \sim Bin(c_{ng}, p_{thin}) \tag{5}$$

where p_{thin} is a specified thinning parameter.

bioRxiv preprint doi: https://doi.org/10.1101/051631; this version posted December 6, 2016. The copyright holder for this preprint (which was not certified by peer review) is the author/funder, who has granted bioRxiv a license to display the preprint in perpetuity. It is made available under aCC-BY-NC-ND 4.0 International license.

Code Availability

Our methods are implemented in an R package `CountClust`, available as part of the Bioconductor project at `https://www.bioconductor.org/packages/3.3/bioc/html/CountClust.html`. The development version of the package is also available at `https://github.com/kkdey/CountClust`.

Code for reproducing results reported here is available at `http://stephenslab.github.io/count-clustering/`.

Acknowledgments

We thank Matt Taddy, Amos Tanay and Effi Kenigsberg for helpful discussions. We thank Po-Yuan Tung, John Blischak and Jonathan Pritchard for helpful comments on the draft manuscript.

bioRxiv preprint doi: https://doi.org/10.1101/051631; this version posted December 6, 2016. The copyright holder for this preprint (which was not certified by peer review) is the author/funder, who has granted bioRxiv a license to display the preprint in perpetuity. It is made available under aCC-BY-NC-ND 4.0 International license.

Table 1. Cluster Annotations GTEx V6 data (with GO annotations).

Cluster	Top 5 Driving Genes	Top significant GO terms (function)[q-value]
1. Royal purple	*NEAT1, IGFBP5, CCLN2, SRSF5, PNISR*	GO:0005654 (nucleoplasm)[2e-10], GO:0044822 (poly-A RNA binding)[3e-09], GO:0044428 (nuclear part)[1e-09], GO:0043233 (organelle lumen)[2e-08]
2. Light purple	*SNAP25, FBXL16, NCDN, SNCB, SLC17A7*	GO:0097458 (neuron part)[2e-25], GO:0007268 (synaptic transmission)[9e-18], GO:0030182 (neuron differentiation)[2e-14], GO:0022008 (neurogenesis)[1e-13], GO:0007267 (cell-cell signaling)[3e-13]
3. Red	*FABP4, PLIN1, FASN, GPX3, LIPE*	GO:0044255 (cellular lipid metabolism)[1e-09], GO:0006629 (lipid metabolism)[1e-09], GO:0006639 (acylglycerol metabolism)[3e-08], GO:0045765 (angiogenesis regulation)[4e-08]
4. Salmon	*ACTG2, MYH11, SYNM, MYLK, CSRP1*	GO:0043292 (contractile fiber)[3e-13], GO:0006936 (muscle contraction)[5e-12], GO:0030016 (myofibril)[5e-12], GO:0015629 (actin cytoskeleton)[2e-12], GO:0005925 (focal adhesion)[6e-11]
5. Denim	*RGS5, MGP, AEBP1, IGFBP7, MFGE8*	GO:0005578 (proteinaceous extracellular matrix)[4e-20], GO:0030198 (extracellular matrix)[2e-18], GO:0007155 (cell adhesion)[4e-14], GO:0001568 (blood vessel development)[4e-13]
6. Light denim	*KRT10, KRT1, KRT2, LOR, KRT14*	GO:0008544 (epidermis development)[3e-12], GO:0043588 (skin development)[5e-10], GO:0042303 (molting cycle)[8e-06], GO:0042633 (hair cycle)[7e-06], GO:0048513 (organ development)[6e-05]
7. Orange	*NEB, MYH1, MYH2, MYBPC1, ACTA1*	GO:0043292 (contractile fiber)[6e-52], GO:0030016 (myofibril)[1e-51], GO:0030017 (sarcomere)[5e-40], GO:0003012 (muscle system process)[2e-25], GO:0015629 (actin cytoskeleton)[1e-25]
8. Light orange	*FN1, COL1A1, COL1A2, COL3A1, COL6A3*	GO:0030198 (extracellular matrix)[6e-29], GO:0043062 (extracellular structure)[4e-29], GO:0032963 (collagen metabolism)[3e-16], GO:0030199 (collagen fibril organization)[1e-14], GO:0030574 (collagen catabolism)[1e-14]
9. Green	*MBP, GFAP, MTURN, HIPK2, CARNS1*	GO:0043209 (myelin sheath)[4e-07], GO:0007399 (nervous system development)[4e-05], GO:0008366 (axon ensheathment)[9e-05], GO:0044430 (cytoskeletal part)[1e-04], GO:0005874 (microtubule)[3e-04]
10. Light green	*CYP17A1, CYP11B1, PIGR, GKN1, STAR*	GO:0006694 (steroid biosynthesis)[2e-13], GO:0008202 (steroid metabolism)[1e-12], GO:0016125 (sterol metabolism)[1e-11], GO:0042446 (hormone biosynthesis)[1e-10], GO:0008207 (C21-steroid hormone metabolism)[3e-10]
11. Turquoise	*MPZ, APOD, PMP22, PRX, NGFR*	GO:0007272 (ensheathment of neurons)[4e-07], GO:0008366 (axon ensheathment)[7e-07], GO:0042552 (myelination)[7e-06], GO:0048856 (anatomical structure development)[1e-06], GO:0005578 (proteinaceous extracellular matrix)[1e-06]
12. Yellow	*IGHM, IGHG1, IGHG2, IGHG4, CD74*	GO:0006955 (immune response)[1e-18], GO:0002252 (immune effector process)[7e-18], GO:0003823 (antigen binding)[1e-15], GO:0019724 (B-cell mediated immunity)[5e-13], GO:0002684 (positive regulation immune system)[6e-13]
13. Sky blue	*TG, PRL, GH1, PRM2, PRM1*	GO:0019953 (sexual reproduction)[8e-10], GO:0048232 (male gamete generation)[2e-08], GO:0035686 (sperm fibrous sheath)[4e-06], GO:0005179 (hormone activity)[6e-05], GO:0042403 (thyroid hormone metabolism)[2e-04]
14. Light pink	*NPPA, MYH6, TNNT2, ACTC1, MYBPC3*	GO:0045333 (cellular respiration)[2e-34], GO:0022904 (respiratory electron transport)[8e-33], GO:0015980 (energy derivation by oxidation of organic compounds)[4e-30], GO:0031966 (mitochondrial membrane)[5e-26]
15. Light gray	*KRT13, KRT4, MUC7, CRNN, KRT6A*	GO:0070062 (extracellular exosome)[2e-23], GO:0043230 (extracellular organelle)[3e-23], GO:0031982 (vesicle)[3e-20], GO:0008544 (epidermis development)[2e-18], GO:0043588 (skin development)[1e-13]
16. Gray	*SFTPBβ, SFTPA1, SFTPA2, SFTPC, A2M*	GO:0001525 (angiogenesis)[5e-08], GO:0001944 (vasculature development)[2e-07], GO:0048514 (blood vessel morphogenesis)[2e-07], GO:0040012 (locomotion regulation)[4e-06], GO:2000145 (cell motility)[1e-05]
17. Brown	*CSF3R, MMP25, IL1R2, SELL, VNN2*	GO:0006955 (immune response)[8e-22], GO:0006952 (defense response)[9e-16], GO:0071944 (cell periphery)[7e-15], GO:0005886 (plasma membrane)[7e-15], GO:0050776 (regulation of immune response)[2e-12]
18. Purple	*PRSS1, CPA1, PNLIP, CELA3A, GP2*	GO:0007586 (digestion)[3e-14], GO:0004252 (serine-type endopeptidase activity)[4e-08], GO:0006508 (proteolysis)[6e-06], GO:0016787 (hydrolase activity)[6e-05], GO:0044241 (lipid digestion)[1e-04]
19. Pink	*HBB, HBA2, HBA1, FKBP8, HBD*	GO:0005833 (hemoglobin complex)[1e-13], GO:0015669 (gas transport)[4e-11], GO:0020037 (heme binding)[3e-07], GO:0031720 (haptoglobin binding)[3e-06], GO:0006950 (response to stress)[6e-04]
20. Dark gray	*ALB, HP, FGB, FGA, ORM1*	GO:0072562 (blood microparticle)[1e-27], GO:0043230 (extracellular organelle)[1e-24], GO:0044710 (single organism metabolism)[7e-20], GO:0019752 (carboxylic acid metabolism)[1e-18], GO:0034364 (high density lipoprotein)[3e-16]

bioRxiv preprint doi: https://doi.org/10.1101/051631; this version posted December 6, 2016. The copyright holder for this preprint (which was not certified by peer review) is the author/funder, who has granted bioRxiv a license to display the preprint in perpetuity. It is made available under aCC-BY-NC-ND 4.0 International license.

Table 2. Cluster Annotations for GTEx V6 Brain data.

Cluster	Top 5 Driving Genes	Top significant GO terms
1. Royal blue	*CLU, OXT, GLUL, NDRG2, CST3*	GO:0043230 (extracellular organelle)[5e-11], GO:1903561 (extracellular vesicle)[6e-11], GO:0070062 (extracellular exosome)[2e-09], GO:0006950 (response to stress)[3e-10], GO:0031988 (membrane bound vesicle)[1e-10]
2. Turquoise	*ENC1, NCALD, YWHAH, KIF5A, NPTXR*	GO:0097458 (neuron part)[3e-11], GO:0008092 (cytoskeletal protein binding)[7e-11], GO:0031175 (neuron projection development)[7e-09], GO:0030182 (neuron differentiation)[4e-08], GO:0007268 (synaptic transmission)[1e-08]
3. Lime green	*PKD1, CBLN3, CHGB, COL27A1, ABLIM1*	GO:0005089 (Rho guanyl-nucleotide exchange factor activity)[1e-03], GO:0016604 (nuclear body)[0.002], GO:0022008 (neurogenesis)[0.02], GO:0035239 (tube morphogenesis)[0.08], GO:0007269 (neurotransmitter secretion)[0.10]
4. Red	*PPP1R1B, RGS14, NCDN, PDE1B, RAP1GAP*	GO:0065009 (regulation of molecular function)[2e-06], GO:0036477 (somatodendritic compartment)[6e-05], GO:0007268 (synaptic transmission)[1e-03], GO:0023051 (signaling regulation)[2e-03], GO:0010646 (cell communication regulation)[1e-03]
5. Yellow orange	*MBP, GFAP, TF, MTURN, SCD*	GO:0043209 (myelin sheath)[2e-09], GO:0007399 (nervous system development)[1e-04], GO:0005737 (cytoplasm)[1e-04], GO:0048471 (perinuclear region of cytoplasm)[5e-04], GO:0007272 (ensheathment of neurons)[1e-02]
6. Yellow	*IQGAP1, A2M, C3, MYH7, TG*	GO:0072562 (blood microparticle)[1e-10], GO:0044449 (contractile fiber part)[1e-10], GO:0043230 (extracellular organelle)[7e-10], GO:0030017 (sarcomere)[1e-08], GO:0072376 (protein activation cascade)[1e-08]

Table 3. Cluster Annotations for Deng et al (2014) data.

Cluster	Top 10 Driving Genes	Top significant GO terms
1. Blue	*Bcl2l10*, *E330034G19Rik*, *Tcl1*,*LOC100502936*, *Oas1d*, *AU022751*, *Spin1*, *Khdc1b*, *D6Ertd527e*, *Btg4*	GO:0007276 (gamete generation)[7e-06], GO:0032504 (multicellular organism reproduction)[3e-06], GO:0044702 (single organism reproduction)[2e-05], GO:0048477 (oogenesis)[5e-04], GO:0048599 (oocyte development)[1e-03], GO:0009994 (oocyte differentiation)[1e-03]
2. Magenta	*Obox3*, *Zfp352*, *Gm8300*, *Usp17l5*, *BB287469*, *Rfpl4b*, *Gm2022*, *Gm5662*, *Gm11544* , *Gm4850*	GO:0016604 (nuclear body)[1e-04], GO:0005814 (centriole)[4e-03], GO:0044450 (microtubule organizing center part) [8e-03]
3. Yellow	*Rtn2*, *Ebna1bp2*, *Zfp259*, *Nasp*, *Cenpe*, *Rnf216*, *Ctsl*, *Tor1b*, *Ankrd10*, *Lamp2*	GO:0044428 (nuclear part)[1e-08], GO:0031981 (nuclear lumen)[3e-08], GO:0070013 (intracellular organelle lumen)[9e-08], GO:0005730 (nucleolus)[5e-07], GO:0005654 (nucleoplasm)[4e-05], GO:0003723 (RNA binding)[1e-04]
4. Green	*Timd2*, *Isyna1*, *Alppl2*, *Prame15*, *Fbxo15*, *Tceb1*, *Gpd1l*, *Pemt*, *Hsp90aa1*, *Hsp90ab1*	GO:0005829 (cytosol)[4e-10], GO:0044444 (cytoplasmic part)[2e-05], GO:1901575 (organic substance catabolic process)[9e-04], GO:0000151 (ubiquitin ligase com- plex)[1e-04], GO:0009056 (catabolic process)[1e-03], GO:0044265 (cellular macromolecule catabolic process)[1e-03], GO:0051082 (unfolded protein binding)[9e-04]
5. Purple	*Upp1*, *Tdgf1*, *Aqp8*, *Fabp5*, *Tat*, *Pdgfra*, *Pyy*, *Prdx1*, *Col4a1*, *Spp1*	GO:0044710 (single-organism metabolic process) [1e-05], GO:0006950 (response to stress) [1e-05], GO:0070062 (extracellular exosome)[1e-05], GO:0043230 (extracellular organelle)[2e-05], GO:1903561 (extracellular vesicle)[1e-05], GO:0006979 (response to oxidative stress)[7e-04], GO:0048514 (blood vessel morphogenesis)[7e-04], GO:0001944 (vasculature development)[3e-03]
6. Orange	*Actb*, *Krt18*, *Fabp3*, *Id2*, *Tspan8*, *Gm2a*, *Lgals1*, *Adh1* , *Lrp2*, *BC051665*	GO:0065010 (extracellular membrane-bounded organelle), GO:0070062 (extracellular exosome)[4e-23], GO:0043230 (extracellular organelle)[5e-23], GO:1903561 (extracellular vesicle)[3e-23], GO:0031982 (vesicle)[4e-18], GO:0030036 (actin cytoskeleton and organization)[4e-12], GO:0032432 (actin filament bundle)[2e-09], GO:0005912 (adherens junction)[2e-09]

bioRxiv preprint doi: https://doi.org/10.1101/051631; this version posted December 6, 2016. The copyright holder for this preprint (which was not certified by peer review) is the author/funder, who has granted bioRxiv a license to display the preprint in perpetuity. It is made available under aCC-BY-NC-ND 4.0 International license.

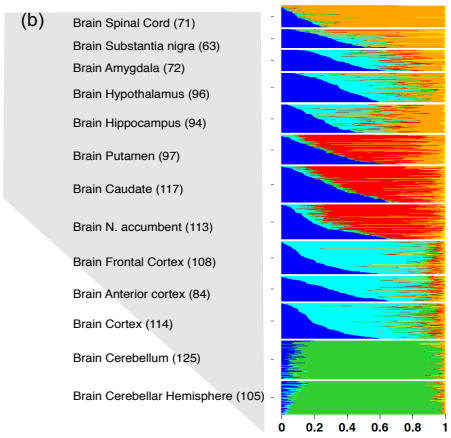

(a) clusters	Top 5 driving genes
1 : Royal Purple	*NEAT1, IGFBP5, CCLN2, SRSF5, PNISR*
2 : Light purple	*SNAP25, FBXL16, NCDN, SNCB, SLC17A7*
3 : Red	*FABP4, PLIN1, FASN, GPX3, LIPE*
4 : Salmon	*ACTG2, MYH11, SYNM, MYLK, CSRP1*
5 : Denim	*RGS5, MGP, AEBP1, IGFBP7, MFGE5*
6 : Light denim	*KRT10, KRT1, KRT2, LOR, KRT14*
7 : Orange	*NEB, MYH1, MYH2, MYBPC1, ACTA1*
8 : Light orange	*FN1, COL1A1, COL1A2, COL3A1, COL6A3*
9 : Green	*MBP, GFAP, MTURN, H1PK2, CARNS1*
10 : Light green	*CYP17A1, CYP11B1, PIGR, GKN1, STAR*
11 : Turquoise	*MPZ, APOD, PMP22, PRX, NGFR*
12 : Yellow	*IGHM, IGHG1, IGHG2, IGHG4, CD74*
13 : Sky blue	*TG, PRL, GH1, PRM2, PRM1*
14 : Light pink	*NPPA, MYH6, TNNT2, ACTC1, MYBPC3*
15 : Light gray	*KRT13, KRT4, MUC7, CRNN, KRT6A*
16 : Gray	*SFTPB, SFTPA1, SFTPA2, SFTPC, A2M*
17 : Brown	*CSF3R, MMP25, IL1R2, SELL, VNN2*
18 : Purple	*PRSS1, CPA1, PNLIP, CELA3A, GP2*
19 : Pink	*HBB, HBA2, HBA1, FKBP8, HBD*
20 : Dark gray	*ALB, HP, FGB, FGA, ORM1*

(b) clusters	Top 5 driving genes
1 : Royal blue	*CLU, OXT, GLUL, NDRG2, CST3*
2 : Turquoise	*ENC1, NCALD, YWHAH, KIF5A, NPTXR*
3 : Lime green	*PKD1, CBLN3, CHGB, COL27A1, ABLIM1*
4 : Bright red	*PPP1R1B, RGS14, NCDN, PDE1B, RAP1GAP*
5 : Yellow orange	*MBP, GFAP, TF, MTURN, SCD*
6 : Yellow	*IQGAP1, A2M, C3, MYH7, TG*

Fig 1. (a): Structure plot of estimated membership proportions for GoM model with $K = 20$ clusters fit to 8555 tissue samples from 53 tissues in GTEx data. Each horizontal bar shows the cluster membership proportions for a single sample, ordered so that samples from the same tissue are adjacent to one another. Within each tissue, the samples are sorted by the proportional representation of the underlying clusters. **(b)**: Structure plot of estimated membership proportions for $K = 4$ clusters fit to only the brain tissue samples. This analysis highlights finer-scale structure among the brain samples that is missed by the global analysis in (a).

bioRxiv preprint doi: https://doi.org/10.1101/051631; this version posted December 6, 2016. The copyright holder for this preprint (which was not certified by peer review) is the author/funder, who has granted bioRxiv a license to display the preprint in perpetuity. It is made available under aCC-BY-NC-ND 4.0 International license.

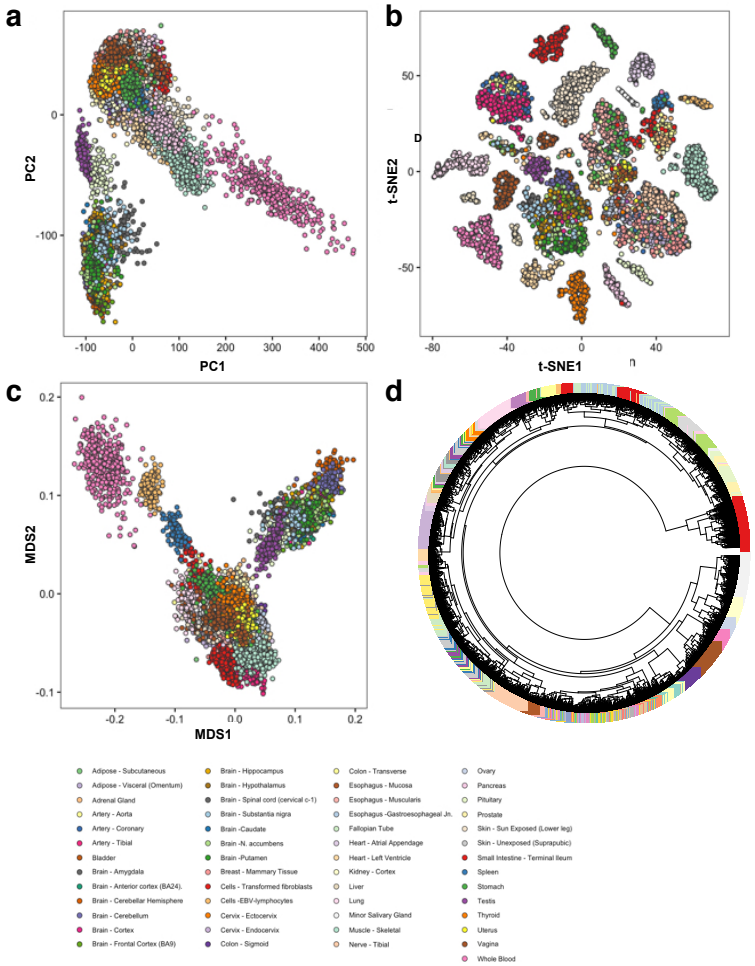

Fig 2. Visualization of the same GTEx data as in Figure 1 (a) across all tissues using standard and widely used approaches - Principal Component Analysis (PCA), Multi dimensional Scaling (MDS), t-SNE and hierarchical clustering. All the analysis are done on log CPM normalized expression data to remove library size effects. **(a)**: Plot of PC1 vs PC2 on the log CPM expression data, **(b)**: Plot of first two dimensions of the t-SNE plot, **(c)** Plot of first two dimensions of the Multi-Dimensional Scaling (MDS) plot. **(d)** Dendrogram for the hierarchical clustring of the GTEx tissue samples based on the log CPM expression data.

bioRxiv preprint doi: https://doi.org/10.1101/051631; this version posted December 6, 2016. The copyright holder for this preprint (which was not certified by peer review) is the author/funder, who has granted bioRxiv a license to display the preprint in perpetuity. It is made available under aCC-BY-NC-ND 4.0 International license.

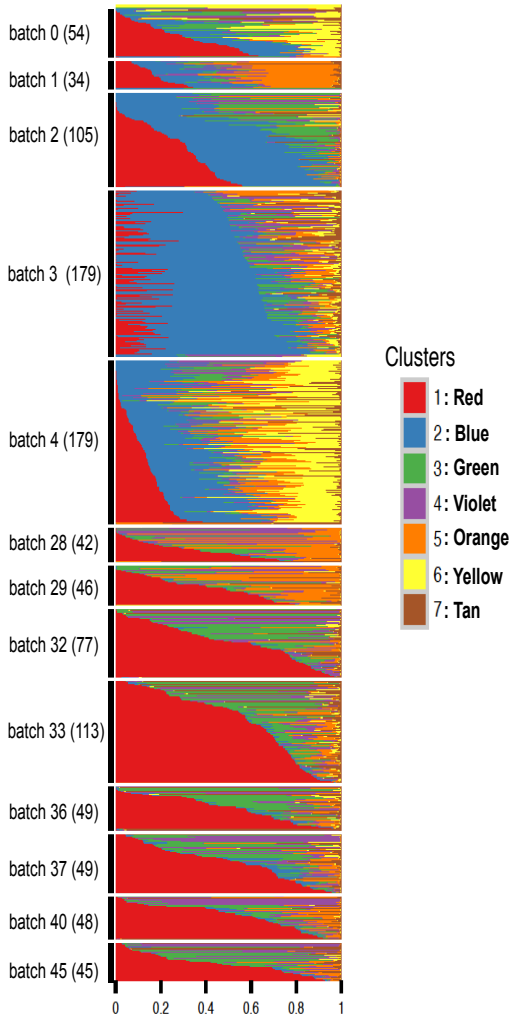

Fig 3. Structure plot of estimated membership proportions for GoM model with $K = 7$ clusters fit to $1,041$ single cells from [27]. The samples (cells) are ordered so that samples from the same amplification batch are adjacent and within each batch, the samples are sorted by the proportional representation of the underlying clusters. In this analysis the samples do not appear to form clearly-defined clusters, with each sample being allocated membership in several "clusters". Membership proportions are correlated with batch, and some groups of batches (e.g. 28-29; 32-45) show similar palettes. These results suggest that batch effects are likely influencing the inferred structure in these data.

bioRxiv preprint doi: https://doi.org/10.1101/051631; this version posted December 6, 2016. The copyright holder for this preprint (which was not certified by peer review) is the author/funder, who has granted bioRxiv a license to display the preprint in perpetuity. It is made available under aCC-BY-NC-ND 4.0 International license.

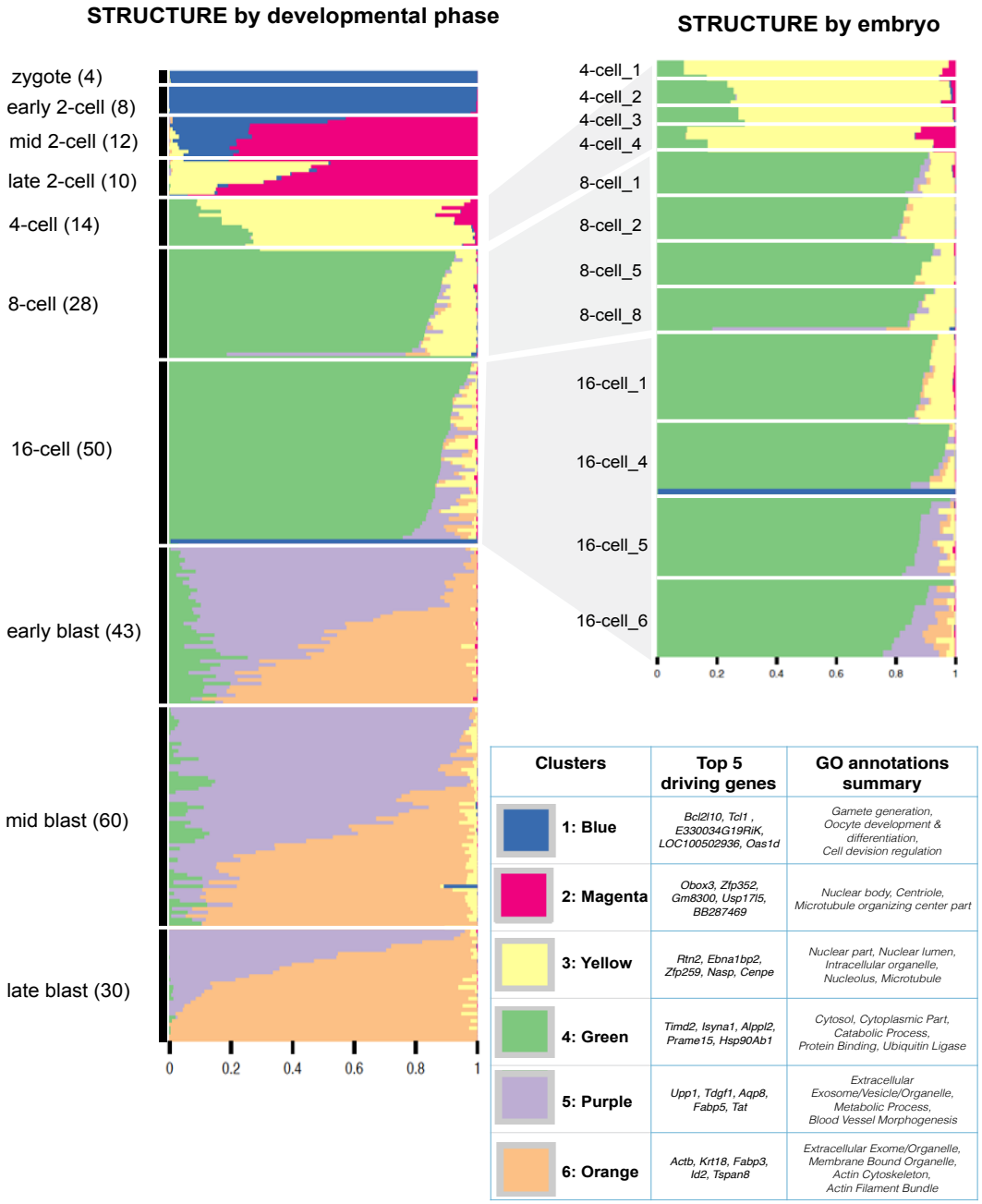

Fig 4. Structure plot of estimated membership proportions for GoM model with $K = 6$ clusters fit to 259 single cells from [28]. The cells are ordered by their preimplantation development phase (and within each phase, sorted by the proportional representation of the clusters). While the very earliest developmental phases (zygote and early 2-cell) are essentially assigned to a single cluster, others have membership in multiple clusters. Each cluster is annotated by the genes that are most distinctively expressed in that cluster, and by the gene ontology categories for which these distinctive genes are most enriched (see Table 3 for more extensive annotation results). See text for discussion of biological processes driving these results.

bioRxiv preprint doi: https://doi.org/10.1101/051631; this version posted December 6, 2016. The copyright holder for this preprint (which was not certified by peer review) is the author/funder, who has granted bioRxiv a license to display the preprint in perpetuity. It is made available under aCC-BY-NC-ND 4.0 International license.

References

1. Guo G, Huss M, Tong GQ, Wang C, SUn LL, Clarke ND, and Robson P. 2010. Resolution of cell fate decisions revealed by single-cell gene expression analysis from zygote to blastocyst. *Developmental Cell*,18(4): 675-685.

2. Rossant J, and Tam PP. 2009. Blastocyst lineage formation, early embryonic assymmetries and axis patterning in the mouse. *Development*,136(5): 701-13.

3. Hernandez MC , Andres-Barquin PJ , Martinez S , Bulfone A , Rubenstein JL , Israel MA. 1997. ENC-1: a novel mammalian kelch-related gene specifically expressed in the nervous system encodes an actin-binding protein. *J Neurosci.*,17(9): 3038-51.

4. Baba H, Nakahira K, Morita N, Tanaka F, Akita H, Ikenaka K. GFAP gene expression during development of astrocyte. *Dev Neurosci.*, 19(1):49-57.

5. Eisen MB, Spellman PT, Brown PO and Botstein D. 1998. Cluster analysis and display of genome-wide expression patterns. *PNAS*, 95(25): 14863-14868

6. Golub TR, Slonim DK, Tamayo P, Huard C, Gaasenbeek M, Mesirov JP, Coller H, Loh ML, Downing JR, Caligiuri MA, Bloomfield CD, Lander ES. 1999. Molecular classification of cancer: class discovery and class prediction by gene expression monitoring. *Science*, 286(5439): 531-7

7. Alizadeh AA1, Eisen MB, Davis RE, Ma C, Lossos IS, Rosenwald A, Boldrick JC *et al.* 2000. Distinct types of diffuse large B-cell lymphoma identified by gene expression profiling. *Nature*, 403(6769): 503-11

8. D'haeseleer P. 2005. How does gene expression clustering work? *Nat Biotechnol*, 23(12):1499-501

9. Jiang D, Tang C, Zhang A. Cluster Analysis for Gene Expression Data: A Survey. *Microsoft Research*, http://research.microsoft.com/en-us/people/djiang/tkde04.pdf.

10. Erosheva EA. 2006. Latent class representation of the grade of membership model. Seattle: University of Washington.

11. Tang F, Barbacioru C, Wang Y, Nordman E, Lee C et al. 2009. mRNA-Seq whole-transcriptome analysis of a single cell. *Nature Methods*, 6, 377 - 382.

12. Trapnell C. 2015. Defining cell types and states with single-cell genomics. *Genome Res.*, 25, 1491-1498.

13. The GTEx Consortium. 2013. The Genotype-Tissue Expression (GTEx) project. *Nature genetics*. 45(6): 580-585. doi:10.1038/ng.2653.

14. Oshlack A, Robinsom MD, Young MD. 2010. From RNA-seq reads to differential expression results. *Genome Biology*. 11:220, DOI: 10.1186/gb-2010-11-12-220

15. Matt Taddy. 2012. On Estimation and Selection for Topic Models. *AISTATS 2012, JMLR W&CP 22*. (maptpx R package).

16. Pritchard, Jonathan K., Matthew Stephens, and Peter Donnelly. 2000. Inference of population structure using multilocus genotype data. *Genetics*. 155.2, 945-959.

bioRxiv preprint doi: https://doi.org/10.1101/051631; this version posted December 6, 2016. The copyright holder for this preprint (which was not certified by peer review) is the author/funder, who has granted bioRxiv a license to display the preprint in perpetuity. It is made available under aCC-BY-NC-ND 4.0 International license.

17. Rosenberg NA, Pritchard JK, Weber JL, Cann HM, Kidd KK, Zhivotovsky LA, Feldman MW. 2002. The genetic structure of human populations. *Science*. 298, 2381-2385.

18. Rosenberg NA. 2005. Algorithms for selecting informative marker panels for population assignment. *J Comput Biol*. 12(9), 1183-201.

19. Raj A, Stephens M, Pritchard JK. 2014. fastSTRUCTURE: Variational Inference of Population Structure in Large SNP Data Sets. *Genetics*. 197, 573-589.

20. Falush D, Stephens M, Pritchard JK. 2003. Inference of population structure using multilocus genotype data: linked loci and correlated allele frequencies. *Genetics*. 164(4), 1567-87.

21. Engelhardt BE, Stephens M. 2010. Analysis of Population Structure: A Unifying Framework and Novel Methods Based on Sparse Factor Analysis. *PLOS Genetics*. DOI: 10.1371/journal.pgen.1001117.

22. Witten DM, Tibshirani R. 2009. A penalized matrix decomposition, with applications to sparse principal components and canonical correlation analysis. *Biostatistics*. 10(3), 515-534.

23. Lopes HF, West M. Bayesian model assessment in factor analysis. *Statistica Sinica*. 14(2004), 41-67

24. Bhattacharya A, Dunson D. Sparse Bayesian infinite factor models. Biometrika (2011). 98(2), 291?306

25. van der Maaten LJP and Hinton GE. 2008. Visualizing High-Dimensional Data Using t-SNE. *J. Mach. Learn. Res.*. 2579-2605.

26. L.J.P. van der Maaten. 2014. Accelerating t-SNE using Tree-Based Algorithms. *J. Mach. Learn. Res.*. 3221-3245.

27. Jaitin DA, Kenigsberg E et al. 2014. Massively Parallel Single-Cell RNA-Seq for Marker-Free Decomposition of Tissues into Cell Types. *Science*. 343 (6172) 776-779.

28. Deng Q, Ramskold D, Reinius B, Sandberg R. 2014. Single-Cell RNA-Seq Reveals Dynamic, Random Monoallelic Gene Expression in Mammalian Cells. *Science*. 343 (6167) 193-196.

29. Leek JT, Storey JD. 2007. Capturing Heterogeneity in Gene Expression Studies by Surrogate Variable Analysis *PLoS Genet*. 3(9): e161. doi:10.1371/journal.pgen.0030161

30. Stegle O, Parts L , Piipari M, Winn J, Durbin R. 2012. Using probabilistic estimation of expression residuals (PEER) to obtain increased power and interpretability of gene expression analyses. *Nat Protoc.*. 7(3):500-7. doi: 10.1038/nprot.2011.457.

31. Leek JT, Scharpf RB, Bravo HC, Simcha D, Langmead B, Johnson WE, Geman D, Baggerly K, Irizarry RA. 2010. Tackling the widespread and critical impact of batch effects in high-throughput data. *Nature Reviews Genetics*. 11, 733-739.

32. Danielsson F and James T and Gomez-Cabrero D and Huss M. 2015. Assessing the consistency of public human tissue RNA-seq data sets. *Briefings in Bioinformatics*. doi :10.1093/bib/bbv017

bioRxiv preprint doi: https://doi.org/10.1101/051631; this version posted December 6, 2016. The copyright holder for this preprint (which was not certified by peer review) is the author/funder, who has granted bioRxiv a license to display the preprint in perpetuity. It is made available under aCC-BY-NC-ND 4.0 International license.

33. Hicks SC, Teng M, Irizarry RA. 2015. On the widespread and critical impact of systematic bias and batch effects in single-cell RNA-Seq data. *BiorXiv*. http://biorxiv.org/content/early/2015/09/04/025528

34. Gilad Y and Mizrahi-Man O. 2015. A reanalysis of mouse ENCODE comparative gene expression data [version 1; referees: 3 approved, 1 approved with reservations]. *F1000Research*. 4:121 (doi: 10.12688/f1000research.6536.1).

35. Mark A, Thompson R and Wu C. 2014. mygene: Access MyGene.Info services. *R package version 1.2.3.*.

36. Gentleman, R., Bates, D., Bolstad, B *et al*. Bioconductor: a software development project. 2003. *Technical Report, Department of Biostatistics, Harvard School of Public Health, Boston*. `https://bioconductor.org/`

37. Flutre T, Wen X, Pritchard J and Stephens M. 2013. A Statistical Framework for Joint eQTL Analysis in Multiple Tissues. *PLoS Genet*. 9(5): e1003486. doi:10.1371/journal.pgen.1003486

38. Shiraishi Y, Tremmel G, Miyano S and Stephens M. 2015. A simple model-based approach to inferring and visualizing cancer mutation signatures. *PLoS Genet*. 11(12): e1005657

39. Diaconis P, Goel S and Holmes S. Horseshoes in multidimensional scaling and local kernel methods. *Ann. Appl. Stat*. 2 (3), 777-807.

40. Novembre J, Stephens M. Interpreting principal component analyses of spatial population genetic variation. *Nat Genet.*. 40 (5), 646-649.

41. Blei DM, Ng AY, Jordan MI. 2003. Latent Dirichlet Allocation. *J. Mach. Learn. Res.*. 3, 993-1022

42. Blei DM, Lafferty J. 2009. Topic Models. *In A. Srivastava and M. Sahami, editors, Text Mining: Classification, Clustering, and Applications . Chapman & Hall/CRC Data Mining and Knowledge Discovery Series*.

43. Shen-Orr SS, Tibshirani R, Khatri, P, Bodian DL, Staedtler F, Perry NM, Hastie, T, Sarwal MM, Davis MM, Butte AJ. 2010. Cell type specific gene expression differences in complex tissues. *Nature Methods*. 7(4), 287-289

44. Qiao W, Quon G, Csaszar E, Yu M, Morris Q, Zandstra PW. 2012. PERT: A Method for Expression Deconvolution of Human Blood Samples from Varied Microenvironmental and Developmental Conditions. *PLoS Comput Biol*. 8(12)

45. Repsilber D, Kern S, Telaar A, Walzl G, Black GF, Selbig J, Parida SK, Kaufmann SH, Jacobsen M. 2010. Biomarker discovery in heterogeneous tissue samples -taking the in-silico deconfounding approach. *BMC bioinformatics*.11(1), 27+

46. Schwartz R, Shackney SE. 2010. Applying unmixing to gene expression data for tumor phylogeny inference. *BMC bioinformatics*. 11(1), 42+

47. Lindsay J, Mandoiu I, Nelson C. 2013. Gene Expression Deconvolution using Single-cells `http://dna.engr.uconn.edu/bibtexmngr/upload/Lal.13.pdf`.

48. Wang N, Gong T, Clarke R, Chen L, Shih IeM, Zhang Z, Levine DA, Xuan J, Wang Y. 2015. UNDO: a Bioconductor R package for unsupervised deconvolution of mixed gene expressions in tumor samples. *Bioinformatics*. 31(1): 137-9

bioRxiv preprint doi: https://doi.org/10.1101/051631; this version posted December 6, 2016. The copyright holder for this preprint (which was not certified by peer review) is the author/funder, who has granted bioRxiv a license to display the preprint in perpetuity. It is made available under aCC-BY-NC-ND 4.0 International license.

49. Ahn J, Yuan Y, Parmigiani G, Suraokar MB, Diao L, Wistuba II, Wang W. DeMix: deconvolution for mixed cancer transcriptomes using raw measured data. 2013. *Bioinformatics*. 29(15): 1865-71

50. Quon G, Haider S, Deshwar AG, Cui A, Boutros PC, Morris Q. Computational purification of individual tumor gene expression profiles leads to significant improvements in prognostic prediction. *Genome Med.*. 5(3): 29

51. Hu JG, Shi LL, Chen YJ, Xie XM, Zhang N, Zhu AY, Zheng JS, Feng YF, Zhang C, Xi J, Lu HZ. 2016. Differential effects of myelin basic protein-activated Th1 and Th2 cells on the local immune microenvironment of injured spinal cord. *Experimental Neurology*. 277, 190-201

52. duVerle D, Tsuda K. 2016. cellTree: Inference and visualisation of Single-Cell RNA-seq data as a hierarchical tree structure. *R package version 1.1.0*, `http://tsudalab.org`.

53. Dey K, Hsiao J, Stephens M. 2016. `CountClust` : Clustering and Visualizing RNA-Seq Expression Data using Grade of Membership Models. *R package version 0.99.3*, `https://www.bioconductor.org/packages/3.3/bioc/html/CountClust.html`

54. Renard M, Callewaert B, Baetens M, Campens L, MacDermot K et al. 2013. Novel MYH11 and ACTA2 mutations reveal a role for enhanced TGFβ signaling in FTAAD *Int J Cardiol*. 165(2), 314-321.

55. Gong B, Cao Z, Zheng P, Vitolo OV, Liu S, Staniszewski A, Moolman D, Zhang H, Shelanski M, Arancio O. 2006. Ubiquitin Hydrolase Uch-L1 Rescues β-Amyloid-Induced Decreases in Synaptic Function and Contextual Memory *Cell*. 126(4), 775-788

56. Hoffman MD, Blei DM, Bach F. 2010. Online learning for latent Dirichlet allocation. *Neural Information Processing Systems*.

57. Kamburov A, et al. 2013. The ConsensusPathDB interaction database: 2013 update. *Nucleic Acids Res*.

58. Pentchev K, et al. 2010. Evidence mining and novelty assessment of protein-protein interactions with the ConsensusPathDB plugin for Cytoscape. *Bioinformatics*.

59. Guo G, Huss M, Tong GQ, Wang C, Sun LL, Clarke ND, Robson P. Resolution of cell fate decisions revealed by single-cell gene expression analysis from zygote to blastocyst. *Developmental Cell*. 18(4), 675-685

60. Rossant, J, Tam PPL. Blastocyst lineage formation, early embryonic asymmetries and axis patterning in the mouse *Development*. 136(5), 701-713, doi: 10.1242/dev.017178

61. Hou J, Charters AM, Lee SC, Zhao Y, Wu, MK, Jones SJM, Marra, MA, Hoodless PA. A systematic screen for genes expressed in definitive endoderm by Serial Analysis of Gene Expression (SAGE). *BMC Developmental Biology*. 7(92), 1-13

62. Yoon S, Kim E, Kim YS, Lee H, Kim K, Bae J, Lee K. Role of Bcl2-like 10 (*Bcl2l10*) in regulating mouse oocyte maturation. *Biology of Reproduction*. 81(3), 497-506.

bioRxiv preprint doi: https://doi.org/10.1101/051631; this version posted December 6, 2016. The copyright holder for this preprint (which was not certified by peer review) is the author/funder, who has granted bioRxiv a license to display the preprint in perpetuity. It is made available under aCC-BY-NC-ND 4.0 International license.

63. Evsikov AV, De Evsikova C. Gene expression during the oocyte-to-embryo transition in mammals. *Molecular Reproduction and Development*. 76, 805-818.

64. Rossant J. Development of the extraembryonic lineages. *Seminars in Developmental Biology*. 6(4), 237-247.

65. Falco G, Lee S, Stanghellini I, Bassey UC, Hamatani T, Ko MSH. Zscan4: a novel gene expressed exclusively in late 2-cell embryos and embryonic stem cells. *Developmental biology*. 307(2), 539-550.

66. Schaniel C, Ang YS, Ratnakumar K, Cormier C, James T, Bernstein E, Lemischka IR, Paddison PJ. Smarcc1/Baf155 couples self-renewal gene repression with changes in chromatic structure in mouse embroynic stem cells. *Stem cells*. 27(12), 2979-91.

67. Putkey FR, Cramer T, Morphew MK, Silk AD, Johnson RS, Mclntosh JR, Cleveland. Unstable Kinetochore-Microtubule capture and chromosomal instability following deletion of CENP-E. *Developmental cells*. 3(3), 351-365.

bioRxiv preprint doi: https://doi.org/10.1101/051631; this version posted December 6, 2016. The copyright holder for this preprint (which was not certified by peer review) is the author/funder, who has granted bioRxiv a license to display the preprint in perpetuity. It is made available under aCC-BY-NC-ND 4.0 International license.

Supporting Information

S1 Fig. Structure plot of GTEx V6 tissue samples for (a) $K = 5$, (b) $K = 10$, (c) $K = 15$, (d) $K = 20$. Some tissues form a separate cluster from the other tissues from $K = 5$ onwards (for example: Whole Blood, Skin), whereas some tissue only form a distinctive subgroup at $K = 20$ (for example: Arteries).

S2 Fig. Top five principal components (PC) for GTEx V6 tissue samples. Scatter plot representation of the top five PCs of the GTEx tissue samples. Data was transformed to log2 counts per million (CPM).

S3 Fig. Comparison between GoM model and hierarchical clustering under different scenarios of data transformation. We used GTEx V6 data for model performance comparisons. Specifically, for every pair of the 53 tissues, we assessed the ability of the methods to separate samples according to their tissue of origin. The subplots of heatmaps show the results of evaluation under different scenarios. Filled squares in the heatmap indicate successful separation of the samples in corresponding tissue pair comparison. (a) Hierarchical clustering on log2 counts per million (CPM) transformed data using Euclidean distance. (b) Hierarchical clustering on the standardized log2-CPM transformed data (transformed values for each gene was mean and scale transformed) using the Euclidean distance. (c) GoM model of $K = 2$ applied to counts. (d) Hierarchical clustering on counts data with the assumption that, for each gene the sample read count c_{ng} has a variance $\bar{c}_g + 1$ that is constant across samples. And, the the gene-specific variance $\bar{c}_g + 1$ was used to scale the distance matrix for clustering. (e) Hierarchical clustering applied to adjusted count data. Each gene has a mean expression value of 0 and variance of 1. Taken together, these results suggest that regardless of the different data transformation scenarios, the GoM model with $K = 2$ is able to separate samples of different tissue of origin, better than hierarchical cluster methods.

S4 Fig. GTEx brain PCA, t-SNE and MDS.

S5 Fig. Structure plot of GTEx V6 tissue samples for $K = 20$ in two runs under different thinning parameter settings. (a) $p_{thin} = 0.01$ and (B) $p_{thin} = 0.0001$. The structure in these two plots closely resemble the pattern observed in Fig 1(a), though there are a few differences from the unthinned version.

S6 Fig. A comparison of accuracy of hierarchical clustering vs GoM on thinned GTEx data, with thinning parameters of $p_{thin} = 0.01$ and $p_{thin} = 0.001$. For each pair of tissue samples from the GTEx V6 data we assessed whether or not each clustering method (with $K = 2$ clusters) separated the samples according to their tissue of origin, with successful separation indicated by a filled square. Thinning deteriorates accuracy compared with the unthinned data (Fig 2), but even then the model-based method remains more successful than the hierarchical clustering in separating the samples by tissue or origin.

S7 Fig. Deng et al (2014) PCA, tSNE, MDS and dendrogram plots for hierarchical clustering.

bioRxiv preprint doi: https://doi.org/10.1101/051631; this version posted December 6, 2016. The copyright holder for this preprint (which was not certified by peer review) is the author/funder, who has granted bioRxiv a license to display the preprint in perpetuity. It is made available under aCC-BY-NC-ND 4.0 International license.

S8 Fig. Additional GoM analysis of Deng et al (2014) data including blastocyst samples and 48 blastocyst marker genes. We considered 48 blastocyst marker genes (as chosen by Guo et al., 2010) and fitted GoM model with $K = 3$ to 133 blastocyst samples. In the Structure plot, blastocyst samples are arranged in order of estimated membership proportion in the Green cluster. The panel located above the Structure plot shows the corresponding pre-implantation stage from which blastocyst samples were collected. The heatmap located below the Structure plot represents expression levels of the 48 blastocyst marker genes (log2 CPM), and the corresponding dendrogram shows results of hierarchical clustering (complete linkage). The table on the right of the expression heatmap displays gene information, showing, from left to right, 1) whether or not the gene is a transcription factor, 2) the driving GoM cluster if the gene was among the top five driving genes, and 3) the featured cell type (TE: trophecoderm, EPI: epiblast, PE: primitive endoderm) that was found in Guo et al., 2010.

S9 Fig. Visualization of PCA and t-SNE results of mouse pre-implantation embryos data from Deng et al (2014) using 48 blastocyst marker genes.

S10 Fig. Sparse Factor Analysis loadings visualization of GTEx V6 tissue samples. The colors represent the 20 different factors. The factor loadings are presented in a stacked bar for each sample. We performed SFA under the scenarios of when the loadings are sparse (left panel) and when the factors are sparse (right panel).

S11 Fig. Sparse Factor Analysis loadings visualization of GTEx brain tissue samples. The colors represent the 6 different factors. The factor loadings are presented in a stacked bar for each sample. We performed SFA under the scenarios of when the loadings are sparse (left panel) and when the factors are sparse (right panel).

S12 Fig. Sparse Factor Analysis loadings visualization of mouse pre-implantation embryos from Deng et al., (2014). The colors represent the 6 different factors. The factor loadings are presented in a stacked bar for each sample. We performed SFA under the scenarios of when the loadings are sparse (left panel) and when the factors are sparse (right panel).

S1 Table. Cluster Annotations of GTEx V6 data with top driving gene summaries.

S2 Table. Cluster Annotations of GTEx V6 Brain data with top driving gene summaries.

S3 Table. Cluster Annotations of Deng data with top driving genes.

S4 Table. Cluster Annotation of Deng data analysis using 48 genes with top driving gene summaries.

bioRxiv preprint doi: https://doi.org/10.1101/051631; this version posted December 6, 2016. The copyright holder for this preprint (which was not certified by peer review) is the author/funder, who has granted bioRxiv a license to display the preprint in perpetuity. It is made available under aCC-BY-NC-ND 4.0 International license.

1 Supplementary figures

S1 Fig. Structure plot of GTEx V6 tissue samples for (A) $K = 5$**, (B)** $K = 10$**, (C)** $K = 15$**, (D)** $K = 20$**.** Some tissues form a separate cluster from the other tissues from $K = 5$ onwards (for example: Whole Blood, Skin), whereas some tissue only form a distinctive subgroup at $K = 20$ (for example: Arteries).

bioRxiv preprint doi: https://doi.org/10.1101/051631; this version posted December 6, 2016. The copyright holder for this preprint (which was not certified by peer review) is the author/funder, who has granted bioRxiv a license to display the preprint in perpetuity. It is made available under aCC-BY-NC-ND 4.0 International license.

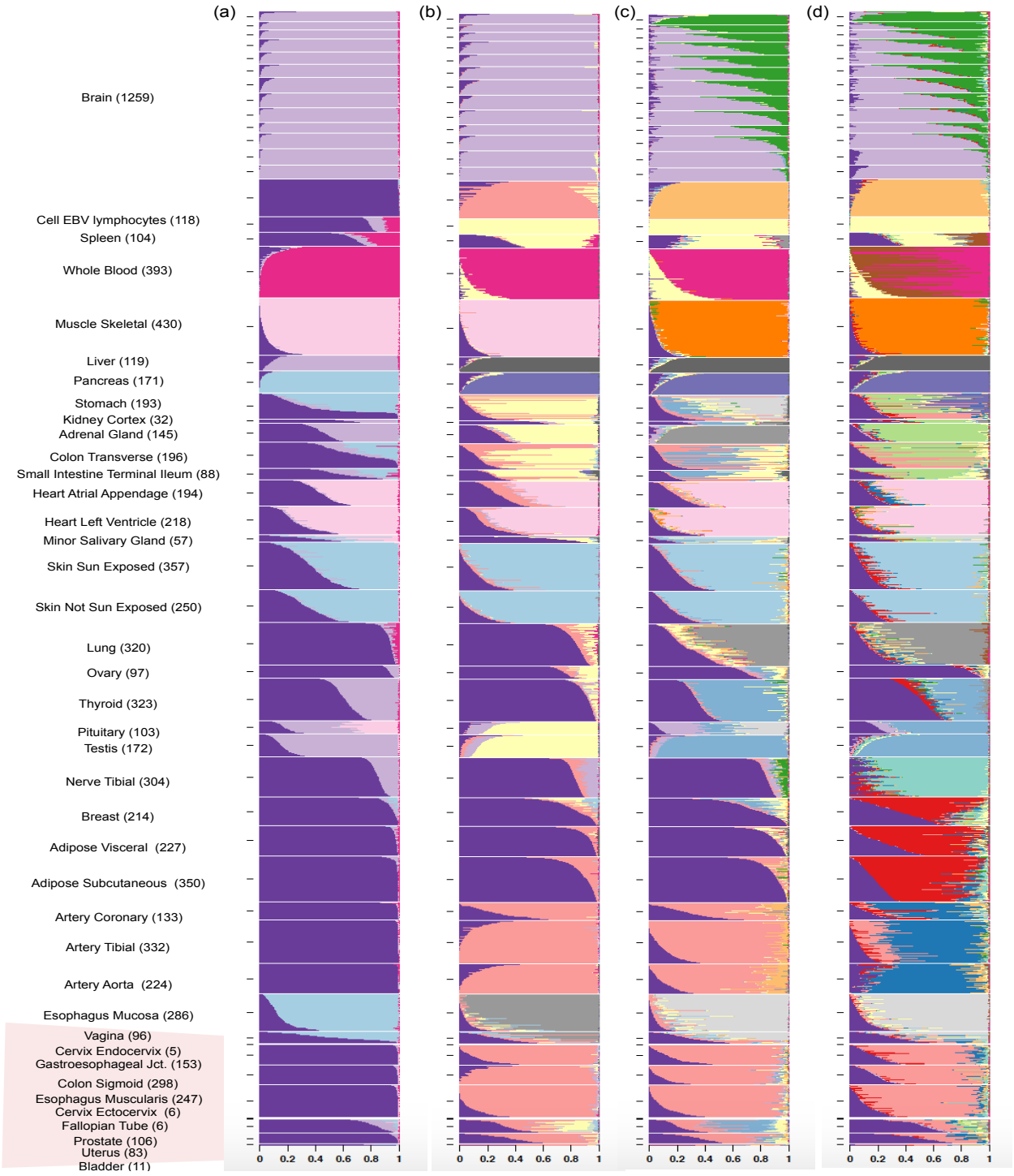

bioRxiv preprint doi: https://doi.org/10.1101/051631; this version posted December 6, 2016. The copyright holder for this preprint (which was not certified by peer review) is the author/funder, who has granted bioRxiv a license to display the preprint in perpetuity. It is made available under aCC-BY-NC-ND 4.0 International license.

S2 Fig. Top five principal components (PC) for GTEx V6 tissue samples. Scatter plot representation of the top five PCs of the GTEx tissue samples. Data was transformed to log2 counts per million (CPM).

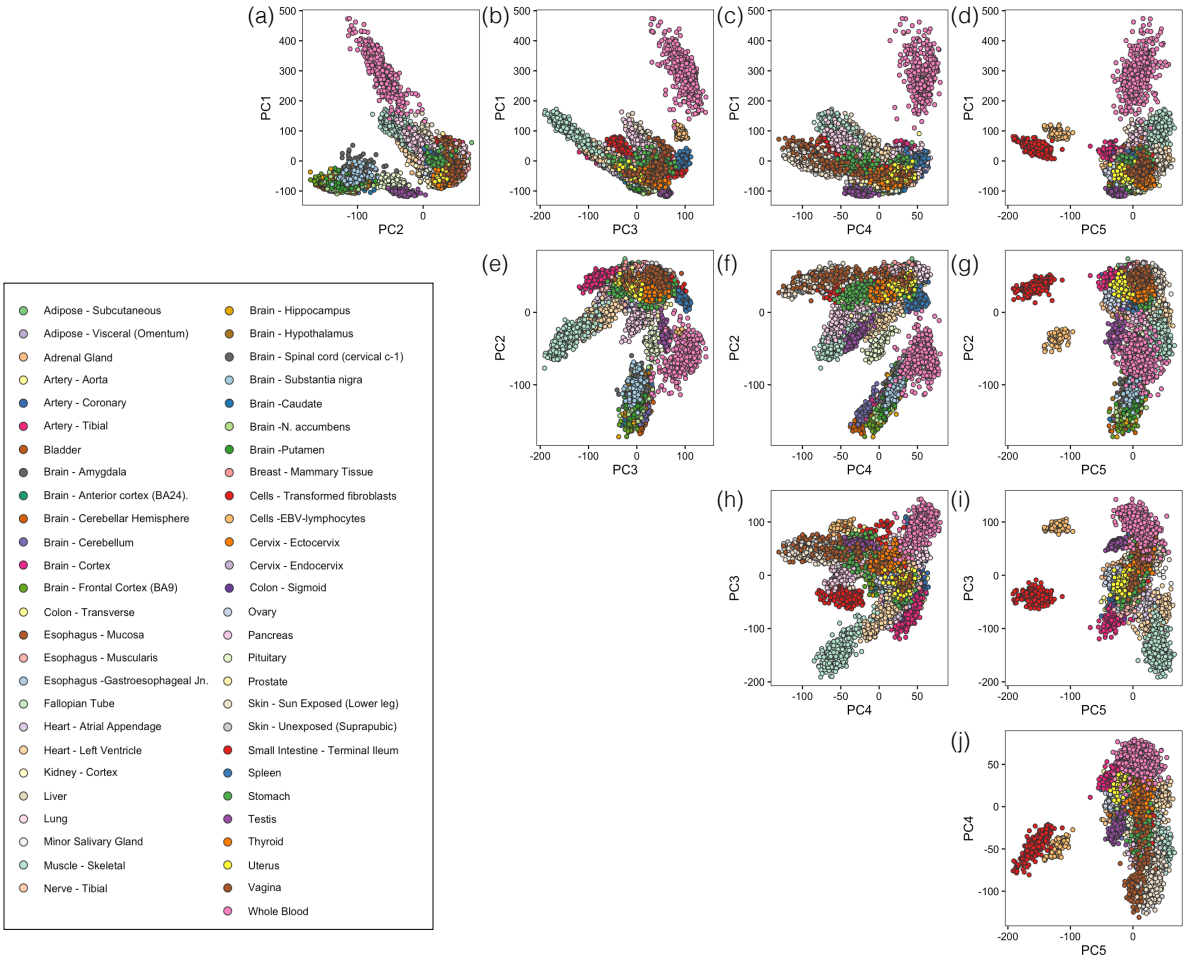

bioRxiv preprint doi: https://doi.org/10.1101/051631; this version posted December 6, 2016. The copyright holder for this preprint (which was not certified by peer review) is the author/funder, who has granted bioRxiv a license to display the preprint in perpetuity. It is made available under aCC-BY-NC-ND 4.0 International license.

S3 Fig. Comparison between GoM model and hierarchical clustering under different scenarios of data transformation. We used GTEx V6 data for model performance comparisons. Specifically, for every pair of the 53 tissues, we assessed the ability of the methods to separate samples according to their tissue of origin. The subplots of heatmaps show the results of evaluation under different scenarios. Filled squares in the heatmap indicate successful separation of the samples in corresponding tissue pair comparison. (a) Hierarchical clustering on log2 counts per million (CPM) transformed data using Euclidean distance. (b) Hierarchical clustering on the standardized log2-CPM transformed data (transformed values for each gene was mean and scale transformed) using the Euclidean distance. (c) GoM model of $K = 2$ applied to counts.(d) Hierarchical clustering on counts data with the assumption that, for each gene the sample read count c_{ng} has a variance $\bar{c}_g + 1$ that is constant across samples. And, the the gene-specific variance $\bar{c}_g + 1$ was used to scale the distance matrix for clustering. (e) Hierarchical clustering applied to adjusted count data from c(c). Each gene expression is further normalized over (c) to have mean expression value of 0 and variance of 1. Taken together, these results suggest that regardless of the different data transformation scenarios, the GoM model with $K = 2$ is able to separate samples of different tissue of origin, better than hierarchical cluster methods.

bioRxiv preprint doi: https://doi.org/10.1101/051631; this version posted December 6, 2016. The copyright holder for this preprint (which was not certified by peer review) is the author/funder, who has granted bioRxiv a license to display the preprint in perpetuity. It is made available under aCC-BY-NC-ND 4.0 International license.

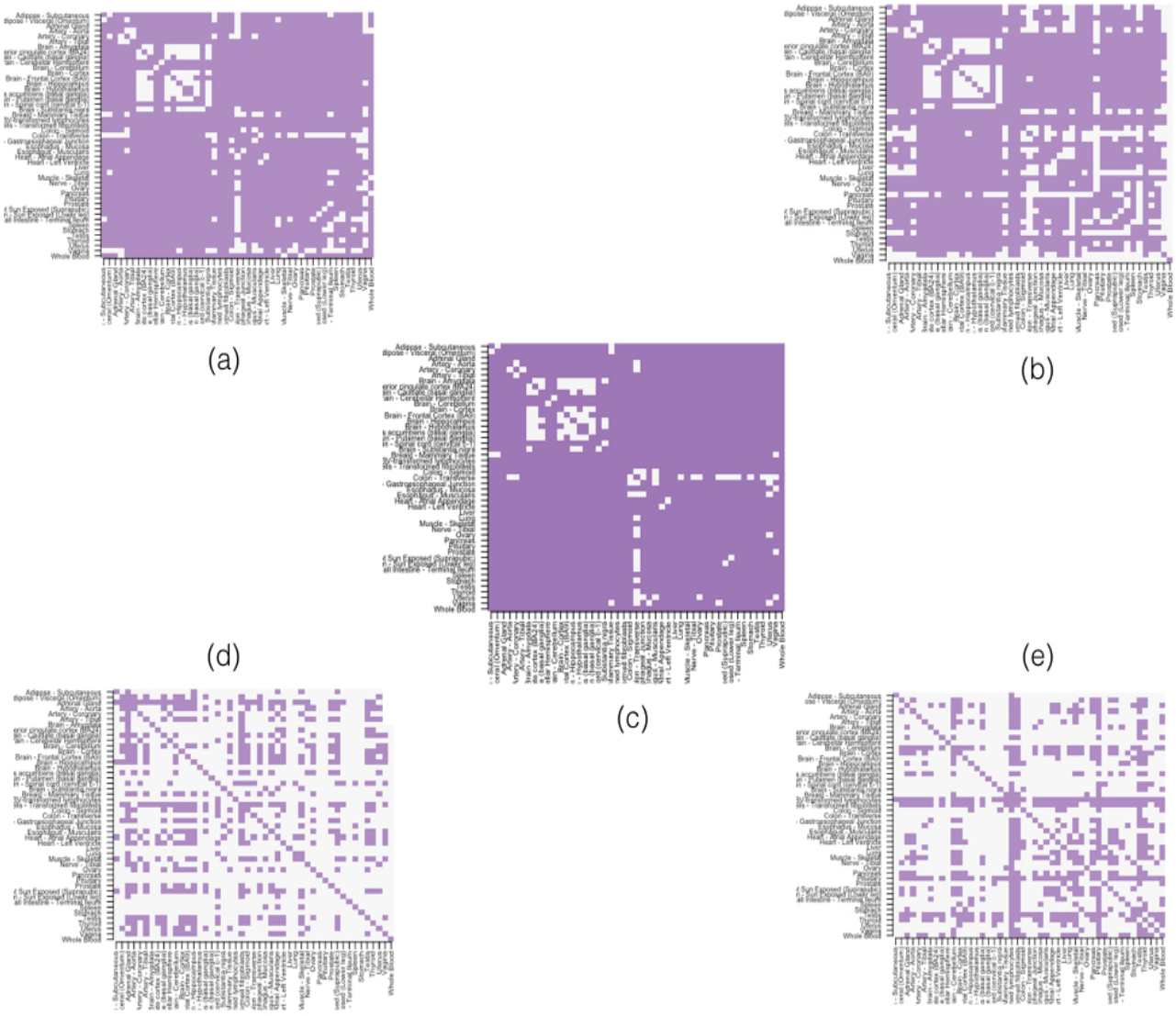

bioRxiv preprint doi: https://doi.org/10.1101/051631; this version posted December 6, 2016. The copyright holder for this preprint (which was not certified by peer review) is the author/funder, who has granted bioRxiv a license to display the preprint in perpetuity. It is made available under aCC-BY-NC-ND 4.0 International license.

S4 Fig. GTEx brain tissue samples visualization using (a) principle component analysis, (b) t-SNE, and (c) Multidimensional scaling and (d) dendrogram for hierarchical clustering. The colors represent the 13 different brain tissue types. In (a) and (b), the majority of the tissue samples are distinct from Cerebellum tissue samples (the cluster of samples located on the right side of the plot). While, in (c), most tissue samples are located at the enter of the plot and are similar to each other in the t-SNE dimensions. In (d), samples from Brain Cerebellar, Cerebellar Hemisphere seem to cluster together and separate from samples from other brain regions. But, because of the large number of samples, patterns of variation between tissue samples are difficult to detect.

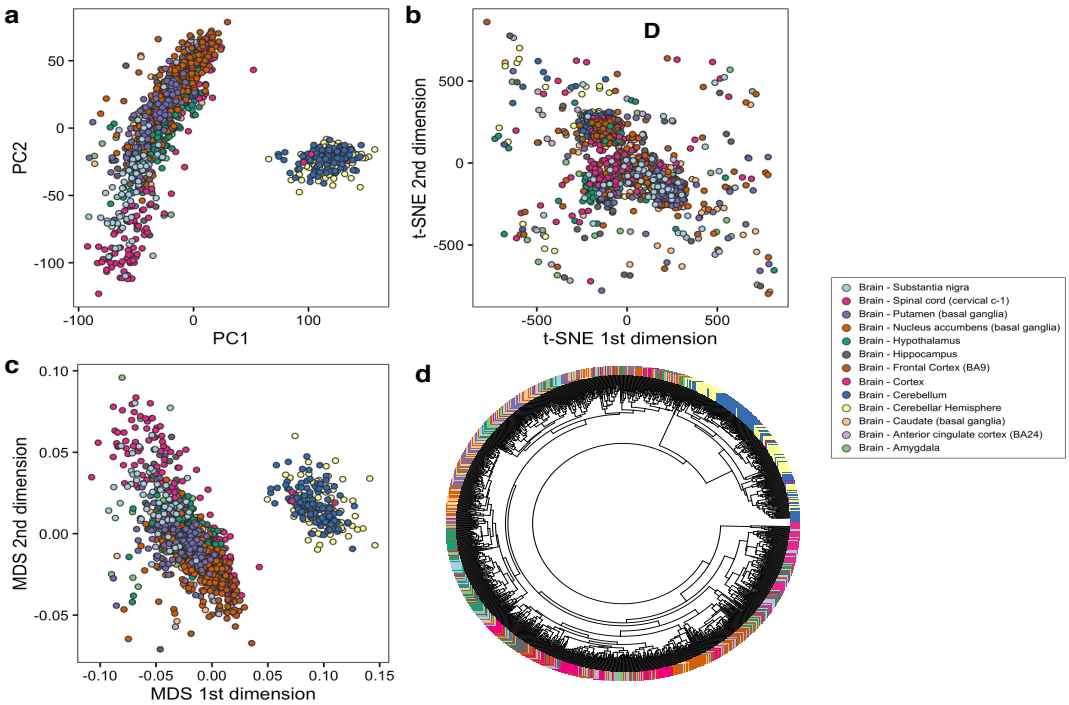

bioRxiv preprint doi: https://doi.org/10.1101/051631; this version posted December 6, 2016. The copyright holder for this preprint (which was not certified by peer review) is the author/funder, who has granted bioRxiv a license to display the preprint in perpetuity. It is made available under aCC-BY-NC-ND 4.0 International license.

S5 Fig. Structure plot of GTEx V6 tissue samples for $K = 20$ in two runs under different thinning parameter settings. (a) $p_{thin} = 0.01$ and (b) $p_{thin} = 0.0001$. The structural patterns in these two plots closely resemble the structural patterns in Fig 1(a), though there are a few differences from the unthinned version.

bioRxiv preprint doi: https://doi.org/10.1101/051631; this version posted December 6, 2016. The copyright holder for this preprint (which was not certified by peer review) is the author/funder, who has granted bioRxiv a license to display the preprint in perpetuity. It is made available under aCC-BY-NC-ND 4.0 International license.

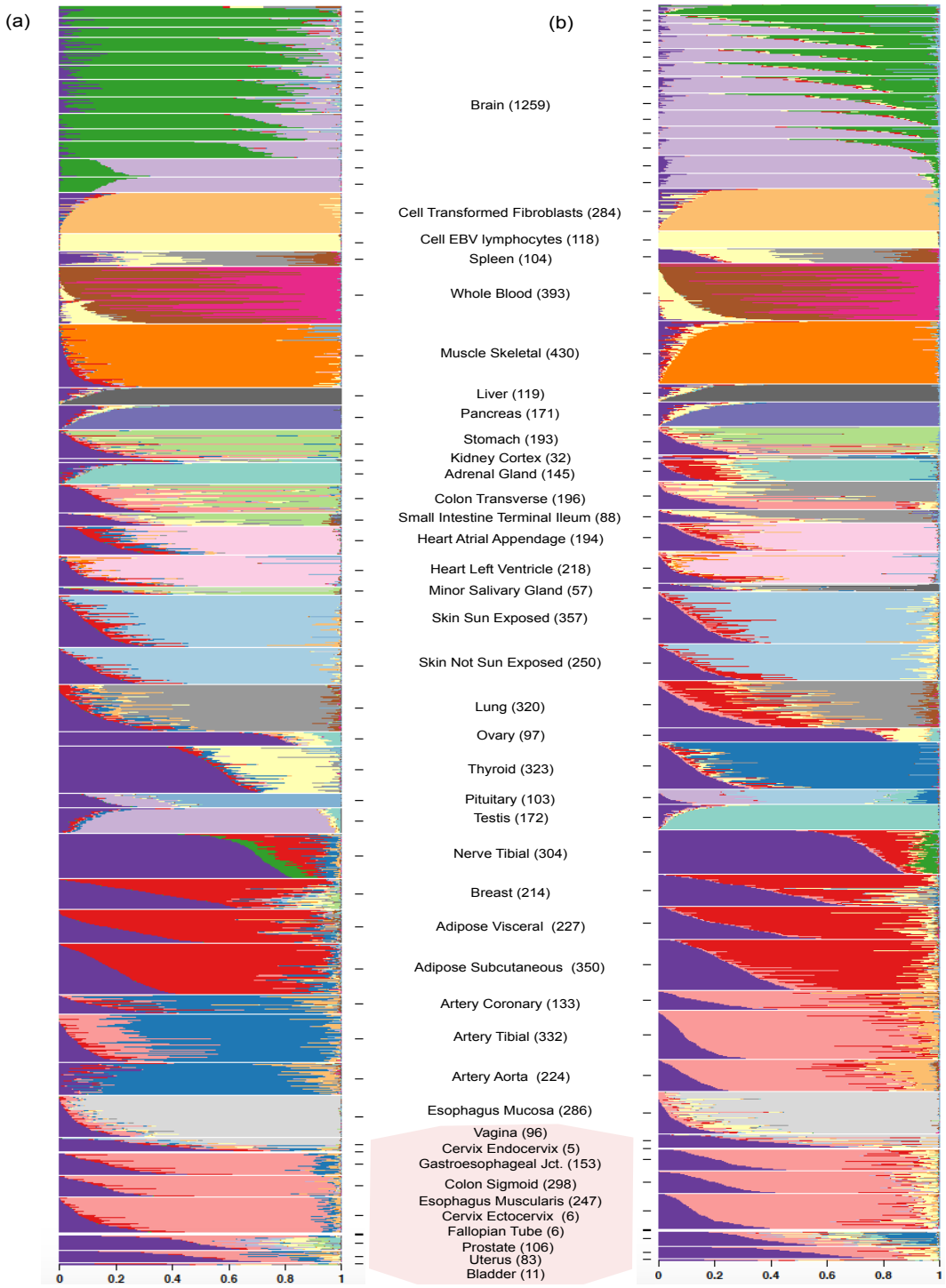

bioRxiv preprint doi: https://doi.org/10.1101/051631; this version posted December 6, 2016. The copyright holder for this preprint (which was not certified by peer review) is the author/funder, who has granted bioRxiv a license to display the preprint in perpetuity. It is made available under aCC-BY-NC-ND 4.0 International license.

S6 Fig. A comparison of "accuracy" of hierarchical clustering vs. GoM on thinned GTEx data, with thinning parameters of $p_{thin} = 0.01$ and $p_{thin} = 0.001$. For each pair of tissue samples from the GTEx V6 data we assessed whether or not each clustering method (with $K = 2$ clusters) separated the samples according to their tissue of origin, with successful separation indicated by a filled square. Thinning deteriorates accuracy compared with the unthinned data (Fig 2), but even then the model-based method remains more successful than the hierarchical clustering in separating the samples by tissue or origin.

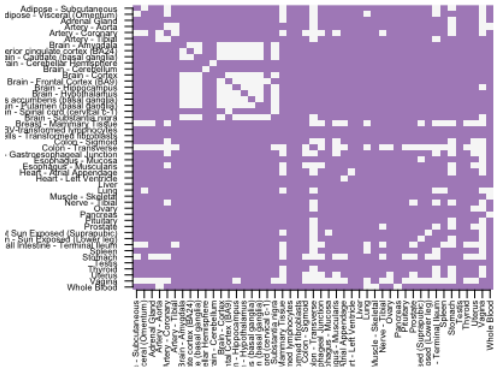

(a) hierarchy thin 0.01

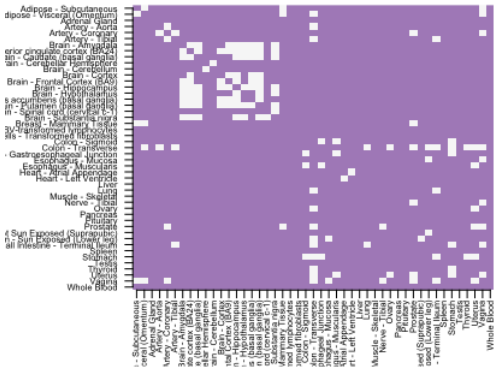

(b) GoM thin 0.01

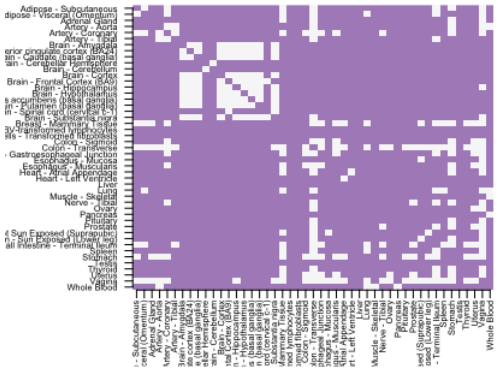

(c) hierarchy 0.001

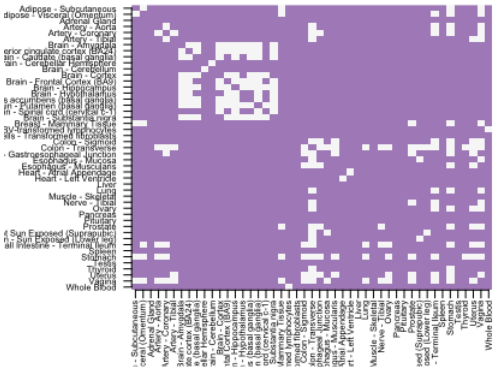

(d) GoM thin 0.001

bioRxiv preprint doi: https://doi.org/10.1101/051631; this version posted December 6, 2016. The copyright holder for this preprint (which was not certified by peer review) is the author/funder, who has granted bioRxiv a license to display the preprint in perpetuity. It is made available under aCC-BY-NC-ND 4.0 International license.

S7 Fig. Visualizing mouse pre-implantation embryos data from Deng et al (2014) using (a) Principle Component Analysis, (b) t-SNE, (c) Multidimensional Scaling (MDS) and (d) circular dendrogram for hierarchical clustering. The colors represent different developmental stages. PCA, MDS seem to be effective in capturing the developmental trajectory, but t-SNE fails to do so. Hierarchical clustering fails to separate out the blastocyst cells from the cells in early stages of development completely.

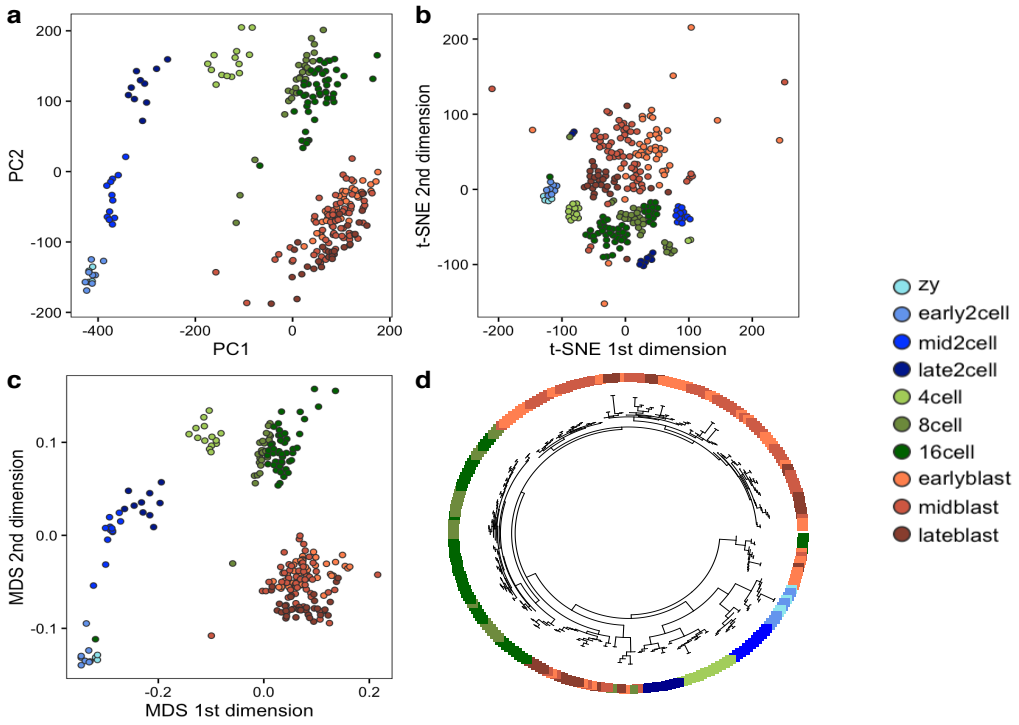

bioRxiv preprint doi: https://doi.org/10.1101/051631; this version posted December 6, 2016. The copyright holder for this preprint (which was not certified by peer review) is the author/funder, who has granted bioRxiv a license to display the preprint in perpetuity. It is made available under aCC-BY-NC-ND 4.0 International license.

S8 Fig. Additional GoM analysis of Deng et al (2014) data including blastocyst samples and 48 blastocyst marker genes. We considered 48 blastocyst marker genes (as chosen by Guo et al., 2010) and fitted GoM model with $K = 3$ to 133 blastocyst samples. In the Structure plot, blastocyst samples are arranged in order of estimated membership proportion in the Green cluster. The panel located above the Structure plot shows the corresponding pre-implantation stage from which blastocyst samples were collected. The heatmap located below the Structure plot represents expression levels of the 48 blastocyst marker genes (log2 CPM), and the corresponding dendrogram shows results of hierarchical clustering (complete linkage). The table on the right of the expression heatmap displays gene information, showing, from left to right, 1) whether or not the gene is a transcription factor, 2) the driving GoM cluster if the gene was among the top five driving genes, and 3) the featured cell type (TE: trophecoderm, EPI: epiblast, PE: primitive endoderm) that was found in Guo et al., 2010.

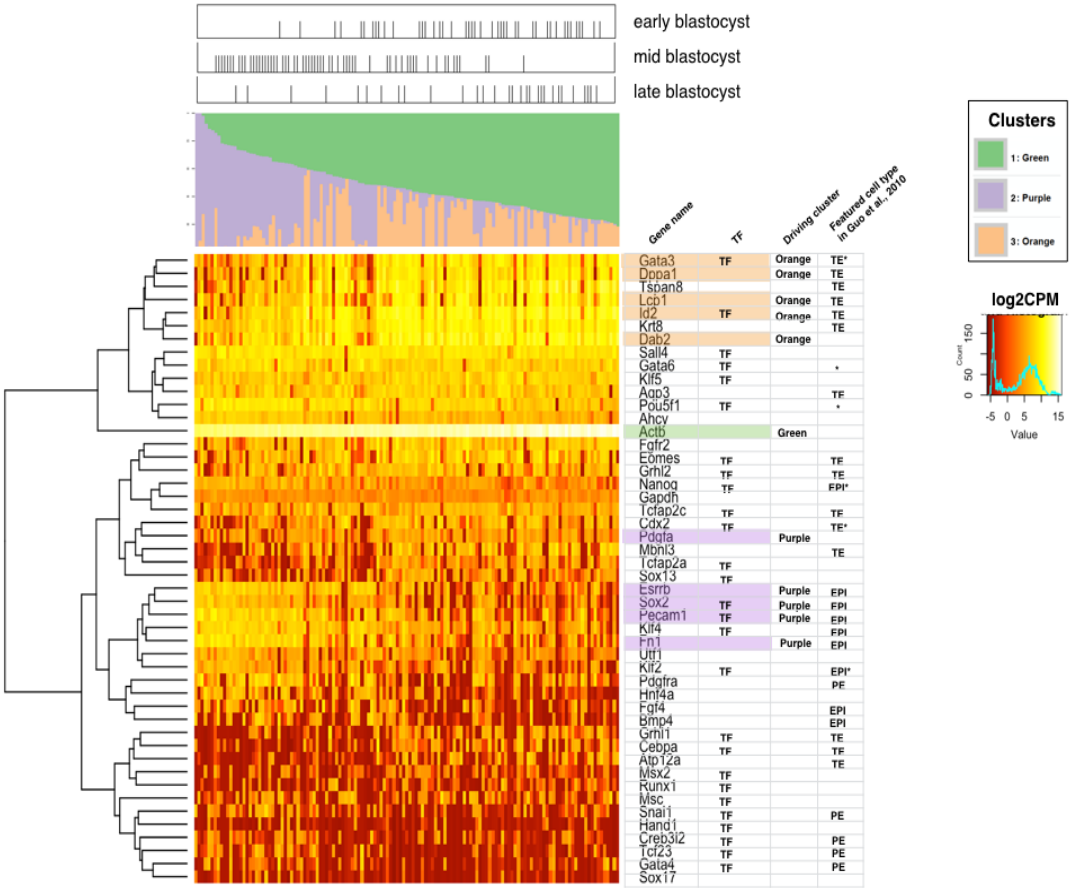

bioRxiv preprint doi: https://doi.org/10.1101/051631; this version posted December 6, 2016. The copyright holder for this preprint (which was not certified by peer review) is the author/funder, who has granted bioRxiv a license to display the preprint in perpetuity. It is made available under aCC-BY-NC-ND 4.0 International license.

S9 Fig. Visualization of PCA and t-SNE results of mouse pre-implantation embryos data from Deng et al (2014) using 48 blastocyst marker genes

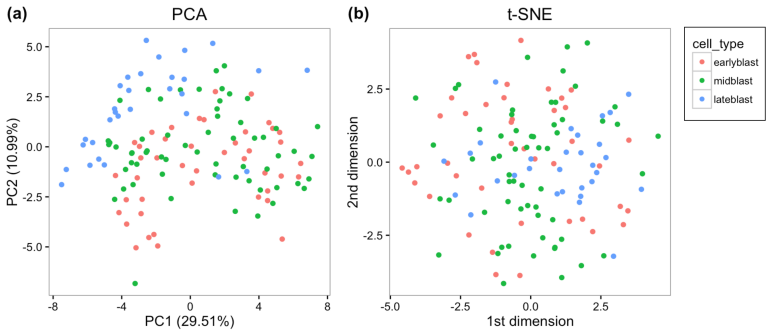

bioRxiv preprint doi: https://doi.org/10.1101/051631; this version posted December 6, 2016. The copyright holder for this preprint (which was not certified by peer review) is the author/funder, who has granted bioRxiv a license to display the preprint in perpetuity. It is made available under aCC-BY-NC-ND 4.0 International license.

S10 Fig. Sparse Factor Analysis loadings visualization of GTEx V6 tissue samples. The colors represent the 20 different factors. The factor loadings are presented in a stacked bar for each sample. We performed SFA under the scenarios of (left) when the loadings are sparse and (right) when the factors are sparse.

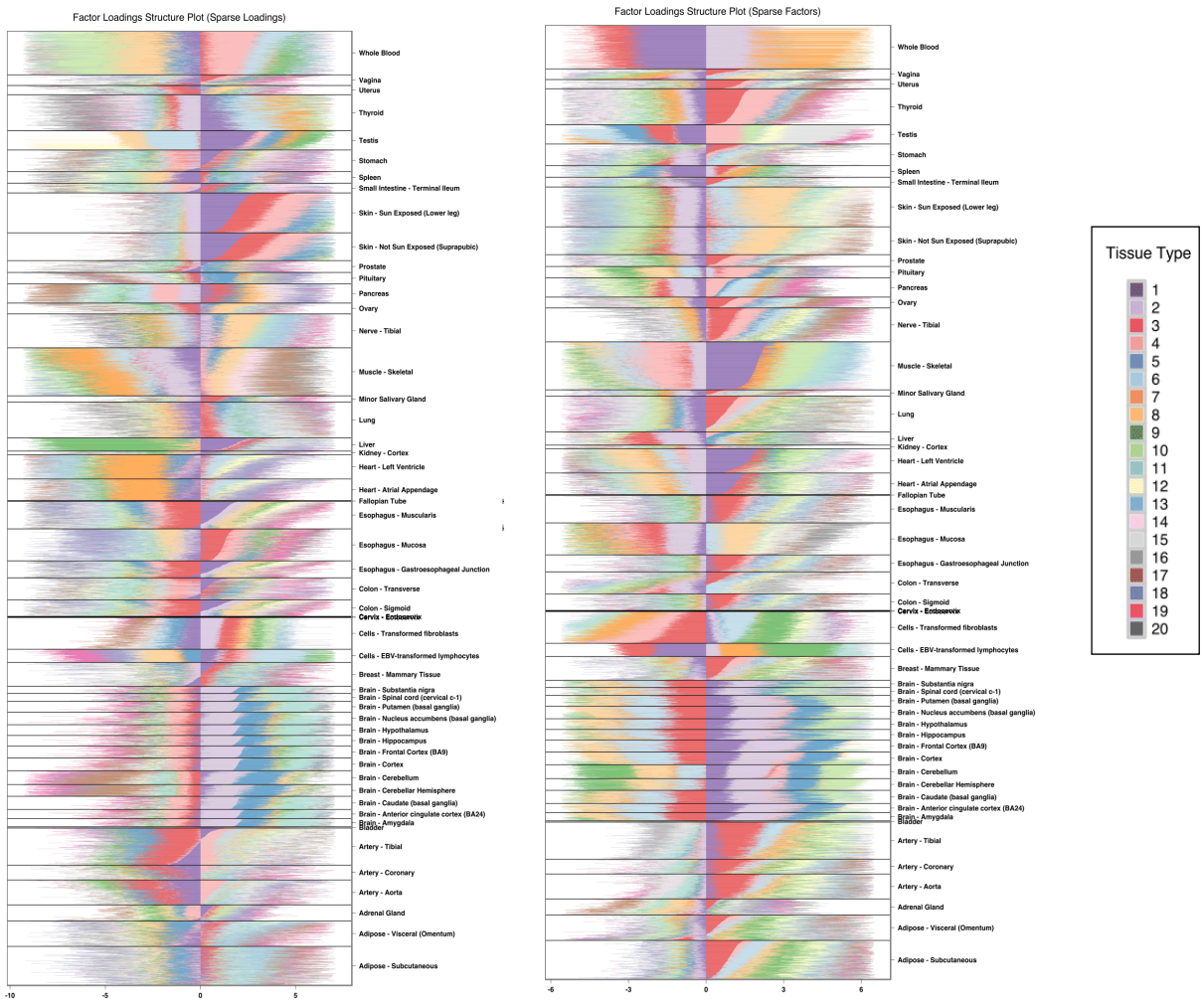

bioRxiv preprint doi: https://doi.org/10.1101/051631; this version posted December 6, 2016. The copyright holder for this preprint (which was not certified by peer review) is the author/funder, who has granted bioRxiv a license to display the preprint in perpetuity. It is made available under aCC-BY-NC-ND 4.0 International license.

S11 Fig. Sparse Factor Analysis loadings visualization of GTEx brain tissue samples. The colors represent the 6 different factors. The factor loadings are presented in a stacked bar for each sample. We performed SFA under the scenarios of (left) when the loadings are sparse and (right) when the factors are sparse.

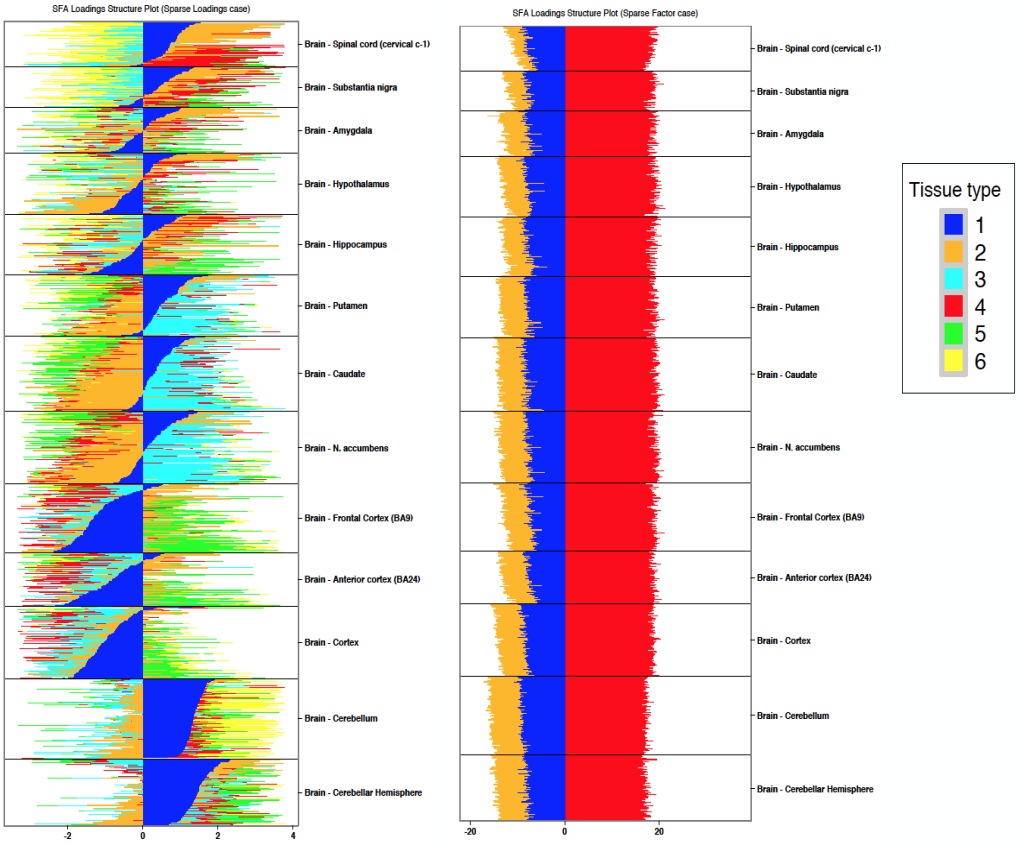

bioRxiv preprint doi: https://doi.org/10.1101/051631; this version posted December 6, 2016. The copyright holder for this preprint (which was not certified by peer review) is the author/funder, who has granted bioRxiv a license to display the preprint in perpetuity. It is made available under aCC-BY-NC-ND 4.0 International license.

S12 Fig. Sparse Factor Analysis loadings visualization of mouse pre-implantation embryos from Deng et al., (2014). The colors represent the 6 different factors. The factor loadings are presented in a stacked bar for each sample. We performed SFA under the scenarios of (left) when the loadings are sparse and (right) when the factors are sparse.

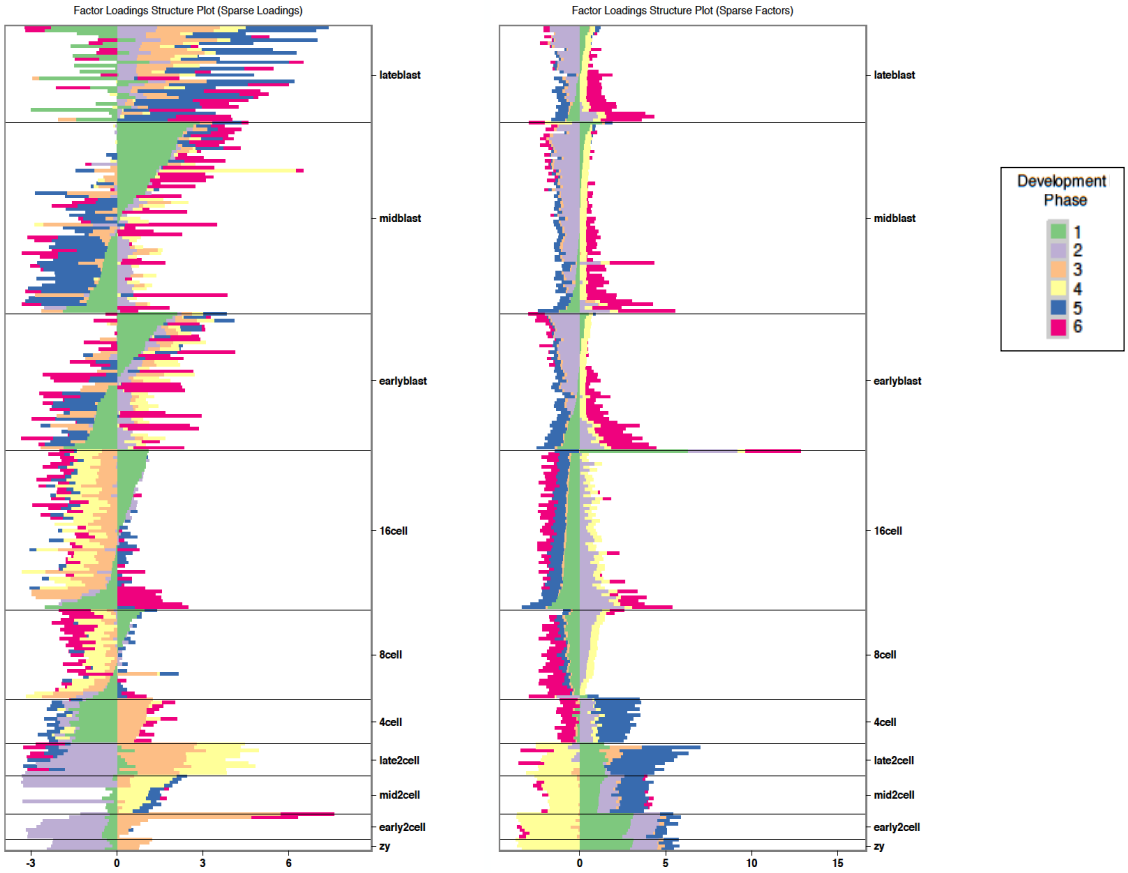

bioRxiv preprint doi: https://doi.org/10.1101/051631; this version posted December 6, 2016. The copyright holder for this preprint (which was not certified by peer review) is the author/funder, who has granted bioRxiv a license to display the preprint in perpetuity. It is made available under aCC-BY-NC-ND 4.0 International license.

2 Supplementary tables

S1 Table. Cluster Annotations of GTEx V6 data with top driving gene summaries.

Cluster	Top Driving Genes	Gene names	Gene Summary
1. Royal purple	*NEAT1*	nuclear paraspeckle assembly transcript 1	produces a long non-coding RNA (lncRNA) transcribed from the multiple endocrine neoplasia locus, regulates genes involved in cancer progression.
	CCNL2	cyclin L2	regulator of the pre-mRNA splicing process, as well as in inducing apoptosis by modulating the expression of apoptotic and antiapoptotic proteins.
	SRSF5	serine/arginine-rich splicing factor 5	encodes proteins of serine/arginine (SR)-rich family, involved in mRNA export from the nucleus and in translation.
2. Light purple	*SNAP25*	synaptosomal-associated protein, 25kDa	this gene product is a presynaptic plasma membrane protein involved in the regulation of neurotransmitter release.
	FBXL16	F-box and leucine-rich repeat protein 16	members of F-box protein family, which interact with SKP1 through the F box, and they interact with ubiquitination targets through other protein interaction domains.
	SLC17A7	neurochondrin	encodes proteins expressed in neuron-rich regions; associated with the membranes of synaptic vesicles and functions in glutamate transport.
3. Red	*FABP4*	fatty acid binding protein 4	encodes the fatty acid binding protein found in adipocytes, takes part in fatty acid uptake, transport, and metabolism.
	PLIN1	perilipin 1	protein encoded by this gene coats lipid storage droplets in adipocytes, thereby protecting them until they can be broken down by hormone-sensitive lipase.
	FASN	fatty acid synthase	catalyze the synthesis of palmitate from acetyl-CoA and malonyl-CoA, in the presence of NADPH, into long-chain saturated fatty acids.
4. Salmon	*ACTG2*	actin, gamma 2, smooth muscle, enteric	involved in various types of cell motility and in the maintenance of the cytoskeleton.
	MYH11	myosin, heavy chain 11, smooth muscle	protein encoded by this gene is a smooth muscle myosin belonging to the myosin heavy chain family, functions as a major contractile protein, converting chemical energy into mechanical energy through the hydrolysis of ATP.
	SYNM	synemin	protein has been found to form a linkage between desmin, which is a subunit of the IF network, and the extracellular matrix, and provides an important structural support in muscle.
5. Denim	*RGS5*	regulator of G-protein signaling 5	encodes a member of the regulators of G protein signaling (RGS) family, associated with retinal arterial macroaneurysm.
	MFGE8	milk fat globule-EGF factor 8 protein	encodes a preproprotein that is proteolytically processed to form multiple protein products, been implicated in wound healing, autoimmune disease, and cancer
	ITGA8	synemin	Proteins generated mediate numerous cellular processes including cell adhesion, cytoskeletal rearrangement, and activation of cell signaling pathways.
6. Light denim	*KRT10*	keratin 10	encodes a member of the type I (acidic) cytokeratin family, mutations associated with epidermolytic hyperkeratosis.
	KRT1	keratin 1, type II	specifically expressed in the spinous and granular layers of the epidermis with family member KRT10 and mutations in these genes have been associated with bullous congenital ichthyosiform erythroderma.
	KRT2	keratin 2, type II	expressed largely in the upper spinous layer of epidermal keratinocytes and mutations in this gene have been associated with bullous congenital ichthyosiform erythroderma.
7. Orange	*NEB*	nebulin	encodes nebulin, a giant protein component of the cytoskeletal matrix that coexists with the thick and thin filaments within the sarcomeres of skeletal muscle, associated with recessive nemaline myopathy.
	MYH1	myosin, heavy chain 1, skeletal muscle, adult	a major contractile protein which converts chemical energy into mechanical energy through the hydrolysis of ATP.
	MYH2	myosin, heavy chain 2, skeletal muscle, adult	encodes a member of the class II or conventional myosin heavy chains, and functions in skeletal muscle contraction.

bioRxiv preprint doi: https://doi.org/10.1101/051631; this version posted December 6, 2016. The copyright holder for this preprint (which was not certified by peer review) is the author/funder, who has granted bioRxiv a license to display the preprint in perpetuity. It is made available under aCC-BY-NC-ND 4.0 International license.

Cluster	Top Driving Genes	Gene namese	Gene Summary
8. Light orange	*FN1*	fibronectin 1	Fibronectin is involved in cell adhesion, embryogenesis, blood coagulation, host defense, and metastasis.
	COL1A1	collagen, type I, alpha 1	Mutations in this gene associated with osteogenesis imperfecta types I-IV, Ehlers-Danlos syndrome type and Classical type, Caffey Disease.
	COL1A2	collagen, type I, alpha 2	Mutations in this gene associated with osteogenesis imperfecta types I-IV, Ehlers-Danlos syndrome type and Classical type, Caffey Disease.
9. Green	*MBP*	myelin basic protein	major constituent of the myelin sheath of oligodendrocytes and Schwann cells in the nervous system
	GFAP	glial fibrillary acidic protein	encodes one of the major intermediate filament proteins of mature astrocytes, mutations casuses Alexander disease.
	CARNS1	carnosine synthase 1	catalyzes the formation of carnosine and homocarnosine, which are found mainly in skeletal muscle and the central nervous system, respectively.
10. Light green	*CYP17A1*	cytochrome P450 family 17 subfamily A member 1	encodes a member of the cytochrome P450 superfamily of enzymes, mutations in this gene are associated with isolated steroid-17 alpha-hydroxylase deficiency,20-lyase deficiency, pseudohermaphroditism, and adrenal hyperplasia.
	CYP11B1	cytochrome P450 family 11 subfamily B member 1	The protein encoded by this gene plays a key role in the acute regulation of steroid hormone synthesis by enhancing the conversion of cholesterol into pregnenolone, associated with congenital lipoid adrenal hyperplasia.
	GKN1	gastrokine 1	protein encoded by this gene is found to be down-regulated in human gastric cancer tissue as compared to normal gastric mucosa..
11. Turquoise	*MPZ*	myelin protein zero	specifically expressed in Schwann cells of the peripheral nervous system and encodes a type I transmembrane glycoprotein that is a major structural protein of the peripheral myelin sheath, mutations associated with autosomal dominant form of Charcot-Marie-Tooth disease type 1 and other polyneuropathies.
	APOD	apolipoprotein D	encodes a component of high density lipoprotein that has no marked similarity to other apolipoprotein sequences, closely associated with lipoprotein metabolism.
	PMP22	peripheral myelin protein 22	encodes an integral membrane protein that is a major component of myelin in the peripheral nervous system..
12. Yellow	*IGHM*	immunoglobulin heavy constant mu	IgM antibodies play an important role in primary defense mechanisms, Diseases associated with IGHM include agammaglobulinemia 1 and immunodeficiency 23.
	IGHG1	immunoglobulin heavy constant gamma 1 (G1m marker)	antigen binding functionality, diseases associated with IGHG1 include heavy chain deposition disease and chronic lymphocytic leukemia.
	IGHG2	immunoglobulin heavy constant gamma 2 (G2m marker)	antigen binding gene, diseases associated with IGHG2 include c2 deficiency.
13. Sky blue	*TG*	thyroglobulin	thyroglobulin produced predominantly in thyroid gland, synthesizes thyroxine and triiodothyronine, associated with Graves disease and Hashimotot thyroiditis.
	PRL	prolactin 2	encodes the anterior pituitary hormone prolactin. This secreted hormone is a growth regulator for many tissues, including cells of the immune system.
	PRM2	protamine 2	Protamines are the major DNA-binding proteins in the nucleus of sperm.
14. Light pink	*NPPA*	natriuretic peptide A	protein encoded by this gene belongs to the natriuretic peptide family, controls extracellular fluid volume and electrolyte homeostasis, mutations Mutations associated with atrial fibrillation familial type 6.
	MYH6	myosin, heavy chain 6, cardiac muscle, alpha	encodes the alpha heavy chain subunit of cardiac myosin, mutations cause familial hypertrophic cardiomyopathy and atrial septal defect 3
	TNNT2	protamine 2	protein encoded by this gene is the tropomyosin-binding subunit of the troponin complex, mutations in this gene have been associated with familial hypertrophic cardiomyopathy as well as with dilated cardiomyopathy.

bioRxiv preprint doi: https://doi.org/10.1101/051631; this version posted December 6, 2016. The copyright holder for this preprint (which was not certified by peer review) is the author/funder, who has granted bioRxiv a license to display the preprint in perpetuity. It is made available under aCC-BY-NC-ND 4.0 International license.

Cluster	Top Driving Genes	Gene namese	Gene Summary
15. Light gray	*KRT13*	keratin 13, type I	protein encoded by this gene is a member of the keratin gene family, associated with the autosomal dominant disorder White Sponge Nevus.
	KRT4	keratin 4, type II	protein encoded by this gene is a member of the keratin gene family, associated with White Sponge Nevus, characterized by oral, esophageal, and anal leukoplakia.
	CRNN	cornulin	may play a role in the mucosal/epithelial immune response and epidermal differentiation.
16. Gray	*SFTPB*	surfactant protein B	an amphipathic surfactant protein essential for lung function and homeostasis after birth, muttaions cause pulmonary alveolar proteinosis, fatal respiratory distress in the neonatal period.
	SFTPA2	surfactant protein A2	Mutations in this gene and a highly similar gene located nearby, which affect the highly conserved carbohydrate recognition domain, are associated with idiopathic pulmonary fibrosis.
	SFTPA1	surfactant protein A1	encodes a lung surfactant protein that is a member of C-type lectins called collectins, associated with idiopathic pulmonary fibrosis.
17. Brown	*CSF3R*	colony stimulating factor 3 receptor	protein encoded by this gene is the receptor for colony stimulating factor 3, a cytokine that controls the production, differentiation, and function of granulocytes, mutations a cause of Kostmann syndrome
	MMP25	matrix metallopeptidase 25	proteins are involved in the breakdown of extracellular matrix in normal physiological processes, such as embryonic development, reproduction, and tissue remodeling, as well as in disease processes, such as arthritis and metastasis.
	IL1R2	interleukin 1 receptor type 2	protein encoded by this gene is a cytokine receptor that belongs to the interleukin 1 receptor family.
18. Purple	*PRSS1*	protease, serine 1	secreted by pancreas, associated with pancreatitis
	CPA1	carboxypeptidase A1	secreted by pancreas, linked to pancreatitis and pancreatic cancer
	PNLIP	pancreatic lipase	encodes a carboxyl esterase that hydrolyzes insoluble, emulsified triglycerides, and is essential for the efficient digestion of dietary fats. This gene is expressed specifically in the pancreas.
19. Pink	*HBB*	hemoglobin, beta	mutant beta globin causes sickle cell anemia, absence of beta chain/ reduction in beta globin leads to thalassemia.
	HBA2	hemoglobin, alpha 2	deletion of alpha genes may lead to alpha thalassemia.
	HBA1	hemoglobin, alpha 1	deletion of alpha genes may lead to alpha thalassemia.
20. Dark gray	*ALB*	albumin	functions primarily as a carrier protein for steroids, fatty acids, and thyroid hormones and plays a role in stabilizing extracellular fluid volume.
	HP	haptoglobin	encodes a preproprotein, which subsequently produces haptoglobin, linked to diabetic nephropathy, Crohn's disease, inflammatory disease behavior and reduced incidence of Plasmodium falciparum malaria.
	FGB	fibrinogen beta chain	protein encoded by this gene is the beta component of fibrinogen, mutations may lead to several disorders, including afibrinogenemia, dysfibrinogenemia, hypodysfibrinogenemia etc.

bioRxiv preprint doi: https://doi.org/10.1101/051631; this version posted December 6, 2016. The copyright holder for this preprint (which was not certified by peer review) is the author/funder, who has granted bioRxiv a license to display the preprint in perpetuity. It is made available under aCC-BY-NC-ND 4.0 International license.

S2 Table. Cluster Annotations of GTEx V6 Brain data with top driving gene summaries.

Cluster	Top Driving Genes	Gene names	Gene Summary
1, Royal blue	*CLU*	clusterin	protein encoded by this gene is a secreted chaperone that can under some stress conditions also be found in the cell cytosol, also involved in cell death, tumor progression, and neurodegenerative disorders.
	OXT	oxytocin/neurophysin I prepropeptide	encodes a precursor protein that is processed to produce oxytocin and neurophysin I, involved in contraction of smooth muscle during parturition and lactation, cognition, tolerance, adaptation and complex sexual and maternal behaviour.
	GLUL	glutamate-ammonia ligase	catalyzes the synthesis of glutamine from glutamate and ammonia in an ATP-dependent reaction, associated with congenital glutamine deficiency, and overexpression of this gene was observed in some primary liver cancer samples.
2, Turquoise	*ENC1*	ectodermal-neural cortex 1	plays a role in the oxidative stress response as a regulator of the transcription factor Nrf2, may play role in malignant transformation.
	NCALD	neurocalcin delta	encodes a member of the neuronal calcium sensor (NCS), a regulator of G protein-coupled receptor signal transduction.
	YWHAH	tyrosine 3-monooxygenase/tryptophan 5-monooxygenase activation protein eta	mediate signal transduction by binding to phosphoserine-containing proteins, associated with early-onset schizophrenia and psychotic bipolar disorder.
3, Lime green	*PKD1*	polycystin 1, transient receptor potential channel interacting	functions as a regulator of calcium permeable cation channels and intracellular calcium homoeostasis. It is also involved in cell-cell/matrix interactions and may modulate G-protein-coupled signal-transduction pathways.
	CBLN3	cerebellin 3 precursor	contain a cerebellin motif and C-terminal C1q signature domain that mediates trimeric assembly of atypical collagen complexes
	CHGB	chromogranin B	encodes a tyrosine-sulfated secretory protein abundant in peptidergic endocrine cells and neurons. This protein may serve as a precursor for regulatory peptides.
4, Red	*PPP1R1B*	protein phosphatase 1 regulatory inhibitor sub- unit 1B	encodes a bifunctional signal transduction molecule, may serve as a therapeutic target for neurologic and psychiatric disorders.
	RGS14	regulator of G-protein signaling 14	attenuates the signaling activity of G-proteins, increases the rate of conversion of the GTP to GDP.
	NCDN	neurochondrin	encodes a leucine-rich cytoplasmic protein, essential for spatial learning processes.
5, Yellow orange	*MBP*	myelin basic protein	protein encoded is a major constituent of the myelin sheath of oligodendrocytes and Schwann cells in the nervous system.
	GFAP	glial fibrillary acidic protein	encodes major intermediate filament proteins of mature astrocytes, a marker to distinguish astrocytes during development, mutations in this gene cause Alexander disease, a rare disorder of astrocytes in central nervous system.
	TF	transferrin	transport iron from the intestine, reticuloendothelial system, and liver parenchymal cells to all proliferating cells in the body, involved in the removal of certain organic matter and allergens from serum.
6, Yellow	*IQGAP1*	IQ motif containing GTPase activating protein 1	interacts with components of the cytoskeleton, with cell adhesion molecules, and with several signaling molecules to regulate cell morphology and motility.
	A2M	alpha-2-macroglobulin	inhibits many proteases, including trypsin, thrombin and collagenase. A2M is implicated in Alzheimer disease (AD) due to its ability to mediate the clearance and degradation of A-beta, the major component of beta-amyloid deposits.
	C3	complement component 3	plays a central role in the activation of complement system, associated with atypical hemolytic uremic syndrome and age-related macular degeneration in human patients.

bioRxiv preprint doi: https://doi.org/10.1101/051631; this version posted December 6, 2016. The copyright holder for this preprint (which was not certified by peer review) is the author/funder, who has granted bioRxiv a license to display the preprint in perpetuity. It is made available under aCC-BY-NC-ND 4.0 International license.

S3 Table. Cluster Annotations of Deng data with top driving genes.

	GO ID	GO Term	Top Driving Genes
1	GO:0007276	gamete generation	BCL2L10; GDF9; NOBOX; PABPC1L; RGS2; CREB3L4; RNF114; BMP15; PTTG1; TDRD12; WEE2; SPIN1; DAZL
2	GO:0007292	female gamete generation	GDF9; BCL2L10; PABPC1L; BMP15; WEE2; DAZL; NOBOX
3	GO:0048609	multicellular organismal reproductive process	GDF9; NOBOX; PABPC1L; BCL2L10; BMP15; CREB3L4; TGFB2; RNF114; RGS2; PTTG1; TDRD12; WEE2; SPIN1; DAZL
4	GO:0032504	multicellular organism reproduction	GDF9; NOBOX; PABPC1L; BCL2L10; BMP15; CREB3L4; TGFB2; RNF114; RGS2; PTTG1; TDRD12; WEE2; SPIN1; DAZL
5	GO:0019953	sexual reproduction	BCL2L10; GDF9; NOBOX; PABPC1L; RGS2; CREB3L4; RNF114; BMP15; PTTG1; TDRD12; WEE2; SPIN1; DAZL
6	GO:0044702	single organism reproductive process	GDF9; NOBOX; PABPC1L; BCL2L10; BMP15; CREB3L4; TGFB2; CASP8; RNF114; RGS2; PTTG1; TDRD12; WEE2; SPIN1; DAZL
7	GO:0048477	oogenesis	WEE2; GDF9; NOBOX; PABPC1L; DAZL
8	GO:0044703	multi-organism reproductive process	BCL2L10; GDF9; NOBOX; PABPC1L; RGS2; CREB3L4; RNF114; BMP15; PTTG1; TDRD12; WEE2; SPIN1; DAZL
9	GO:0048599	oocyte development	WEE2; GDF9; PABPC1L; DAZL
10	GO:0009994	oocyte differentiation	WEE2; GDF9; PABPC1L; DAZL
11	GO:0051321	meiotic cell cycle	H1FOO; WEE2; TDRD12; SPIN1; PTTG1; DAZL
12	GO:0001556	oocyte maturation	WEE2; PABPC1L; DAZL
13	GO:0006306	DNA methylation	TDRD12; H1FOO; TET3; ZFP57
14	GO:0051302	regulation of cell division	TGFB2; PTTG1; TXNIP; WEE2; CHEK1; DAZL
15	GO:0060255	regulation of macromolecule metabolic process	TGFB2; NOBOX; BPGM; UBE2D3; NFYA; CASP8; BMP15; TXNIP; TDRD12; GDF9; BCL2L10

S3 Table continued. Deng et al (2014) Cluster 2 (magenta) top GO annotations.

	GO ID	GO Term	Top Driving Genes
1	GO:0016604	nuclear body	YTHDC1; RBM8A; CDK12; PSME4; PPP1R8; HIPK1; TOPORS
2	GO:0005814	centriole	SFI1; PLK2; ROCK1; TOPORS
3	GO:0044450	microtubule organizing center part	SFI1; PLK2; ROCK1; TOPORS

bioRxiv preprint doi: https://doi.org/10.1101/051631; this version posted December 6, 2016. The copyright holder for this preprint (which was not certified by peer review) is the author/funder, who has granted bioRxiv a license to display the preprint in perpetuity. It is made available under aCC-BY-NC-ND 4.0 International license.

S3 Table continued. Deng et al (2014) Cluster 3 (yellow) top GO annotations.

	GO ID	GO Term	Top Driving Genes
1	GO:0044428	nuclear part	MAD2L2; SMARCC1; PPRC1; SLU7; NFYB; TOR1B; MIOS; NR1H3; POLR3K
2	GO:0031981	nuclear lumen	MAD2L2; SMARCC1; PPRC1; SLU7; NFYB; POLR1E; MIOS; POLR3K; XPO1
3	GO:0070013	intracellular organelle lumen	MAD2L2; SMARCC1; PPRC1; SLU7; NFYB; POLR1E; MIOS; POLR3K; XPO1; DNTTIP2; ZBTB10; ZBTB17
4	GO:0043233	organelle lumen	MAD2L2; SMARCC1; PPRC1; SLU7; NFYB; POLR1E; MIOS; POLR3K; XPO1
5	GO:0005730	nucleolus	XPO1; DNTTIP2; ESF1; WDR43; ZDHHC7; HEATR1; POLR1E; DDX24; POLR3K
6	GO:0005634	nucleus	MAD2L2; SMARCC1; PPRC1; SLU7; NFYB; TOR1B; MIOS; NR1H3; EIF5B; POLR3K
7	GO:0044446	intracellular organelle part	MAD2L2; PTDSS2; SMARCC1; KLHL21; TOR1B; PPRC1; SLU7; NFYB; SLC25A36; ECE2
8	GO:0005654	nucleoplasm	MAD2L2; SMARCC1; PPRC1; SLU7; NFYB; POLR1E; MIOS; POLR3K; XPO1; ZBTB10; ZBTB17
9	GO:0003723	RNA binding	PPRC1; EIF5B; XPO1; DNTTIP2; WDR43; DDX10; EIF3C; BCLAF1; EBNA1BP2; RARS
10	GO:0003676	nucleic acid binding	SMARCC1; PPRC1; SLU7; NFYB; POLR1E; EIF5B; POLR3K; XPO1; DNTTIP2
11	GO:0043231	intracellular membrane-bounded organelle	MAD2L2; PTDSS2; SMARCC1; TOR1B; PPRC1; SLU7; NFYB; ESF1; ECE2; LMAN1L
12	GO:0043229	intracellular organelle	MAD2L2; PTDSS2; SMARCC1; KLHL21; TOR1B; PPRC1; ARRDC1; SLU7; NFYB; ESF1; ECE2
13	GO:0005874	microtubule	WDR43; KLHL21; HAUS6; CENPE; TEKT2; RACGAP1; WDR81; BCL2L11; KIF20B
14	GO:0044822	poly(A) RNA binding	WDR43; DNTTIP2; ESF1; NXF1; DDX10; HEATR1; EIF3C
15	GO:0044424	intracellular part	MAD2L2; PTDSS2; SMARCC1; KLHL21; TOR1B; PPRC1; SNAPC4; POLR3K; ARRDC1; SLU7; NFYB; ESF1; WDR43; ECE2; LMAN1L

bioRxiv preprint doi: https://doi.org/10.1101/051631; this version posted December 6, 2016. The copyright holder for this preprint (which was not certified by peer review) is the author/funder, who has granted bioRxiv a license to display the preprint in perpetuity. It is made available under aCC-BY-NC-ND 4.0 International license.

S3 Table continued. Deng et al (2014) Cluster 4 (green) top GO annotations.

	GO ID	GO Term	Top Driving Genes
1	GO:0005829	cytosol	PARG; UAP1; PSMB10; TCEB1; RPLP0; EIF5; CNBP; RPS3; PSAT1; AACS; PMM1; EXOSC7; EIF3I; SET; BHMT; BHMT2
2	GO:0044444	cytoplasmic part	PARG; UAP1; PSMB10; TCEB1; HSPA8; SERINC1; EIF5; CNBP; RPS3; PSAT1; GPD2; AACS; GPR137B; STIP1; PMM1; EXOSC7; VPREB3; PEX16
3	GO:0055131	C3HC4-type RING finger domain binding	HSPA8; PINK1; DNAJA1
4	GO:1901575	organic substance catabolic process	PSMB10; TCEB1; RPLP0; RPS3; GPD2; PINK1; EXOSC7; ALLC; BHMT; HSP90AB1; RPL13A; ATG7; CUL5; UBXN1; ZMPSTE24
5	GO:0000151	ubiquitin ligase complex	DNAJA1; RNF7; UBE2C; HSPA8; FBXO15; SUGT1; DCAF4; CUL5; FBXL20
6	GO:0072655	protein localization to mitochondrion	TIMM17A; BNIP3L; ARIH2; PEMT; SFN; PINK1; HSP90AA1; TIMM23
7	GO:1901564	organonitrogen compound metabolic process	PSMB10; RPLP0; SERINC1; EIF5; BHMT2; PINK1; EIF3I; ALLC; BHMT; MRPL22; RPL13A; ATG7; NUDT9; VNN1; CTSA; HK1
8	GO:0005737	cytoplasm	PARG; UAP1; PSMB10; TCEB1; HSPA8; SERINC1; EIF5; CNBP; RPS3; PSAT1; GPD2; AACS; GPR137B; STIP1; PMM1; EXOSC7
9	GO:0044265	cellular macromolecule catabolic process	EXOSC7; SUMO2; BNIP3L; ARIH2; PSMB10; TCEB1; RPLP0; UBXN1; HSP90AB1; RPL13A; RPS3; RNF7; PINK1
10	GO:0023026	MHC class II protein complex binding	HSP90AB1; HSP90AA1; HSPA8
11	GO:0051082	unfolded protein binding	DNAJA1; PTGES3; HSPA8; HSP90AB1; HSP90AA1; NPM1
12	GO:0009056	catabolic process	PSMB10; TCEB1; RPLP0; RPS3; GPD2; PINK1; EXOSC7; ALLC; WDR45; HSP90AB1; RPL13A
13	GO:0009057	macromolecule catabolic process	EXOSC7; SUMO2; BNIP3L; ARIH2; PSMB10; TCEB1; RPLP0; AZIN1; UBXN1; HSP90AB1; RPL13A
14	GO:0044248	cellular catabolic process	PSMB10; TCEB1; SUMO2; RPS3; GPD2; PINK1; EXOSC7; ALLC; WDR45; HSP90AB1
15	GO:0006626	protein targeting to mitochondrion	TIMM17A; BNIP3L; ARIH2; PEMT; PINK1; HSP90AA1; TIMM23

bioRxiv preprint doi: https://doi.org/10.1101/051631; this version posted December 6, 2016. The copyright holder for this preprint (which was not certified by peer review) is the author/funder, who has granted bioRxiv a license to display the preprint in perpetuity. It is made available under aCC-BY-NC-ND 4.0 International license.

S3 Table continued. Deng et al (2014) Cluster 5 (purple) top GO annotations.

	GO ID	GO Term	Top Driving Genes
1	GO:0044710	single-organism metabolic process	PCK2; SAT1; EPHX2; NFATC4; CKB; PRDX6; MSH2; EPHA4; PROS1; PDGFRA; PRDX1; UBE2L6; POGLUT1; FABP5; AKAP12; TDGF1; FBP2; SOX2
2	GO:0006950	response to stress	EPHX2; NFATC4; PRDX6; MSH2; EPHA4; PROS1; PDGFRA; PRDX1; UBE2L6; FABP5; TDGF1; SOX2
3	GO:0065010	extracellular membrane-bounded organelle	PCK2; EPHX2; MFGE8; CKB; PRDX6; PROS1; PRDX1; POGLUT1; FABP5; FBP2; TRAP1; PLOD2; DHRS4
4	GO:0070062	extracellular exosome	PCK2; EPHX2; MFGE8; CKB; PRDX6; PROS1; PRDX1; POGLUT1; FABP5; FBP2; TRAP1; PLOD2; DHRS4; MARCKS; DPP4; PRKCI; RAC2; IDH1
5	GO:0043230	extracellular organelle	PCK2; EPHX2; MFGE8; CKB; PRDX6; PROS1; PRDX1; POGLUT1; FABP5; FBP2; TRAP1; PLOD2; DHRS4; MARCKS; DPP4
6	GO:1903561	extracellular vesicle	PCK2; EPHX2; MFGE8; CKB; PRDX6; PROS1; PRDX1; POGLUT1; FABP5; FBP2; TRAP1; PLOD2; DHRS4; MARCKS; DPP4; PRKCI
7	GO:0042221	response to chemical	EPHX2; NFATC4; MFGE8; PRDX6; EPHA4; PROS1; PDGFRA; PRDX1; UBE2L6; TDGF1; SOX2
8	GO:0031988	membrane-bounded vesicle	PCK2; EPHX2; MFGE8; CKB; PRDX6; PROS1; PRDX1; POGLUT1; FABP5; FBP2; TRAP1; PLOD2; DHRS4; SPARC
9	GO:0031982	vesicle	PCK2; EPHX2; MFGE8; CKB; PRDX6; PROS1; PRDX1; POGLUT1; FABP5; FBP2; TRAP1; PLOD2; DHRS4; SPARC
10	GO:0001525	angiogenesis	SAT1; PDGFRA; BMP4; NFATC4; MFGE8; FN1; MEIS1; SPARC; COL4A2; COL4A1; FGF10; TDGF1
11	GO:0048514	blood vessel morphogenesis	SAT1; PDGFRA; BMP4; NFATC4; MFGE8; FN1; ZFP36L1; MEIS1; SPARC; COL4A2; COL4A1; FGF10; TDGF1
12	GO:0001944	vasculature development	SAT1; PDGFRA; BMP4; NFATC4; MFGE8; FN1; ZFP36L1; MEIS1; PDPN; SPARC; COL4A2; COL4A1; FGF10; TDGF1
13	GO:0006979	response to oxidative stress	TAT; PDGFRA; BMP4; ETV5; TRAP1; PRDX6; IDH1; PARP1; AQP8; PRDX1; CRYGD
14	GO:0009725	response to hormone	PRKCI; GJA1; PDGFRA; BMP4; MFGE8; TAT; PLOD2; SPP1; IDH1
15	GO:0030198	extracellular matrix organization	PDGFRA; BMP4; JAM2; FN1; PLOD2; SPARC; SPP1; COL4A2; COL4A1; SERPINH1; DPP4

bioRxiv preprint doi: https://doi.org/10.1101/051631; this version posted December 6, 2016. The copyright holder for this preprint (which was not certified by peer review) is the author/funder, who has granted bioRxiv a license to display the preprint in perpetuity. It is made available under aCC-BY-NC-ND 4.0 International license.

S3 Table continued. Deng et al (2014) Cluster 6 (orange) top GO annotations.

	GO ID	GO Term	Top Driving Genes
1	GO:0065010	extracellular membrane-bounded organelle	MYH10; SLC2A3; GM2A; TSPAN8; ACTG1; SDC4; TINAGL1; CRYAB; MSN; FABP3; PDZK1IP1; PRSS8; S100A11; DAB2; KRT8; LCP1; UGP2
2	GO:0070062	extracellular exosome	MYH10; SLC2A3; GM2A; TSPAN8; ACTG1; SDC4; TINAGL1; CRYAB; MSN; FABP3; PDZK1IP1; PRSS8; S100A11; DAB2; KRT8; LCP1; UGP2
3	GO:0043230	extracellular organelle	MYH10; SLC2A3; GM2A; TSPAN8; ACTG1; SDC4; TINAGL1; CRYAB; MSN; FABP3; PDZK1IP1; PRSS8; S100A11
4	GO:1903561	extracellular vesicle	MYH10; SLC2A3; GM2A; TSPAN8; ACTG1; SDC4; TINAGL1; CRYAB; MSN; FABP3; PDZK1IP1; PRSS8; S100A11; DAB2; KRT8
5	GO:0031988	membrane-bounded vesicle	MYH10; SLC2A3; GM2A; TSPAN8; ACTG1; TMSB4X; SDC4; TINAGL1; CRYAB; MSN; FABP3; PDZK1IP1; PRSS8; S100A11; DAB2
6	GO:0031982	vesicle	MYH10; SLC2A3; GM2A; TSPAN8; ACTG1; TMSB4X; SDC4; TINAGL1; CRYAB; MSN; FABP3; PDZK1IP1; PRSS8; S100A11; DAB2; KRT8
7	GO:0008092	cytoskeletal protein binding	MYH10; TPM4; TMSB4X; CRYAB; MSN; TMSB10; FABP3; NDRG1; CALM1; FMNL2; MYH9; CAP1; TPM1; CDH1
8	GO:0015629	actin cytoskeleton	MYH10; CLIC4; MYH9; MYL12B; WDR1; CNN2; ARPC2; AHNAK; ACTN4; CRYAB; CAP1; TPM1; DSTN; ARPC5; TPM4
9	GO:0003779	actin binding	MYH10; TPM4; WDR1; CNN2; FMNL2; ARPC2; MYH9; CAP1; TPM1
10	GO:0048468	cell development	MYH10; CAPG; ACTG1; WDR1; CNN2; FMNL2; MYH9; ACTN4; SDC4; CAP1; TPM1; DSTN
11	GO:0030036	actin cytoskeleton organization	MYH10; CAPG; ACTG1; WDR1; CNN2; FMNL2; MYH9; ACTN4; SDC4; CAP1; TPM1
12	GO:0032432	actin filament bundle	MYH10; TPM4; MYL12B; CNN2; MYH9; CRYAB; TPM1; ACTN4; LCP1
13	GO:0005912	adherens junction	TJP2; MYH9; ACTG1; CNN2; ARPC2; AHNAK; ACTN4; SDC4
14	GO:0070161	anchoring junction	TJP2; MYH9; ACTG1; CNN2; ARPC2; AHNAK; ACTN4; SDC4
15	GO:0005925	focal adhesion	MYH9; ACTG1; CNN2; ARPC2; AHNAK; ACTN4; SDC4; CAP1; ARPC5

bioRxiv preprint doi: https://doi.org/10.1101/051631; this version posted December 6, 2016. The copyright holder for this preprint (which was not certified by peer review) is the author/funder, who has granted bioRxiv a license to display the preprint in perpetuity. It is made available under aCC-BY-NC-ND 4.0 International license.

S4 Table. Cluster Annotation of Deng data analysis using 48 genes with top driving gene summaries.

Cluster	Top 5 Driving Genes	Top significant GO terms (function)[q-value]
Green	*Actb*	GO:0048568 (embryonic organ development)[9e-08], GO:0048468 (cell development)[4e-07], GO:0001890 (placenta development)[1e-06], GO:0051094 (positive regulation of developmental process)[1e-06], GO:0030097 (hemopoiesis)[1e-05]
Purple	*Pecam1, Esrrb, Fn1, Pdgfra, Sox2*	GO:0048864 (stem cell development)[4e-12], GO:0048863 (stem cell differentiation)[2e-11], GO:0009893 (positive regulation of metabolic process)[7e-10], GO:0009653 (anatomical structure morphogenesis)[4e-08]
Orange	*Dppa1, Gata3, Id2, Dab2, Lcp1*	GO:0061061 (muscle structure development)[2e-13], GO:0060537 (muscle tissue development)[2e-12], GO:0048514 (blood vessel morphogenesis)[8e-12], GO:0007275 (multocellular orgasnimal development)